A Lagrangian approach for the coupled simulation of fixed net structures in a Eulerian fluid model

Tobias Martin* Arun Kamath Hans Bihs

Department of Civil and Environmental Engineering, Norwegian University of Science and Technology (NTNU), 7491 Trondheim, Norway

Postprint
published in *Journal of Fluids and Structures*, 2020, Vol. **94**,
DOI: 10.1016/j.jfluidstructs.2020.102962.

Abstract

A Lagrangian approach for the coupled numerical simulation of fixed net structures and fluid flow is derived. The model is based on solving the Reynolds-averaged Navier-Stokes equations in a Eulerian fluid domain. The equations include disturbances to account for the presence of the net. For this purpose, forces on the net are calculated using a screen force model and are distributed on Lagrangian points to represent the geometry of the net. In comparison to previous approaches based on porous media representations, the new model includes a more physical derivation and simplifies the necessary numerical procedure. Hence, it is also suitable for arbitrary geometries and large scale simulations. An extensive validation section provides insight into the performance of the new model. It includes the simulation of steady currents through single and multiple fixed net panels and cages, and wave propagation through a net panel. Different solidities, inflow velocities and angles of attack are considered. The comparison of loads on and velocity reductions behind the net with available measurements indicates superior performance of the proposed model over existing approaches for a wide range of applications.

Keywords: Hydroelasticity, Net structure, Fluid-structure interaction, CFD, Drag forces

1 Introduction

Aquaculture has seen strong growth recently due to its potential for covering the rising global food demand. Offshore fish production becomes relevant as the size of the structures increases and greater concerns about the environmental impact on the nearshore zone arise. In the open sea, severe environmental loadings from high energy sea states necessitate the accurate analysis of motion and fatigue for the design of reliable and economical fish farm structures.

*Corresponding author, tobias.martin@ntnu.no

The enclosure of a fish cage consists of a large number of square or rhombic meshes forming a flexible or stiff net cylinder or panel. Patursson et al. [29] performed measurements of drag and lift forces on a fixed net panel and the velocity reduction behind the net for different inflow velocities and angles of attack. They observed that the force coefficients are more dependent on the angle of attack than on the Reynolds number and that the velocity reduction is less dependent on the angle of attack. Similarly, Bi et al. [5] conducted experiments on the velocity profile behind multiple net panels in a current tank. Their results indicate that the velocity reduction behind the net is a function of the net solidity due to a changing shielding effect. In [6], an experimental study on the deformation of a net wall in different current velocities was presented. Lader and Enerhaug [21] analysed the forces and deformation of a complete net cage in a current. They found a strong coupling between occurring forces and deformation and concluded that existing simple drag formulae for stiff net panels are not suitable for calculating the forces on flexible cage structures. Less research is focused on experiments including waves. Lader et al. [23, 24] studied wave forces on net panels in a small wave flume and compared the results with different wave force models. They showed the increasing influence of the net on the wave forces with increasing wave steepness. A complete study of a net cage in current and waves including an elastic floater, mooring and net was presented in [19], where the authors investigated the validity of different rational hydrodynamic load models for more complex wave situations.

Besides experimental studies, numerical simulations using computational fluid dynamics (CFD) can be applied to understand the structural and environmental challenges in the operation of the whole structure. It allows for the investigation of the forces on and the fluid dynamics in and around the cage. Mostly separate numerical studies on either the motion of the structure or the fluid around the structure were performed in the past [15, 22, 36]. However, a segregated approach is not valid for offshore conditions due to the strong non-linear fluid-structure interaction. Resolving a physical net in a computational domain which also covers the surrounding ocean is not feasible considering the significant difference in length scales and the available computational power. One possibility to overcome this limitation is the application of the potential theory which is based on disproportional assumptions [19]. The introduction of an advanced procedure which decouples the resolution dependence of the fluid from the net representation is eventually the more elaborated and efficient solution. Here, the introduction of an appropriate coupling model is the main issue of concern.

Yao et al. [38] presented a hybrid finite volume method to incorporate the fluid-structure coupling into their CFD solver. The resistance forces of the net were distributed by assigning them to cells containing portions of the numerical net. The net was represented by a lumped mass method consisting of knots and bars in between. The distribution process requires the calculation of the intersection of each bar with each cell of the fluid grid and is thus computationally expensive. This drawback is amplified for rectilinear grids and polyhedral cell shapes where intersections can only be found by comparison to each cell face. They also introduced the idea of choosing the unknown force coefficients by fitting them with experimental data. Details about the fitting process and fitting results for the drag coefficients were not presented. In contrast, the most dominant approach is based on the work of Patursson et al. [29]. They incorporated a stiff net sheet as a porous medium in the fluid domain. The governing volume- and Reynolds-averaged Navier-Stokes equations are solved using a finite volume method. The research was mostly focused on the correct determination of the porous resistance coefficients, which were approximated from available experimental data. Bi et al.

[6] and Zhao et al. [40] followed the same approach but used a theoretical force model for determining the coefficients. Chen and Christensen [11, 12] extended the general idea for complete net cages and included a more comprehensive determination of these coefficients. They provided an extensive validation of their approach for stiff net walls and cages in both current and waves. A Morison type force model which neglects important dependencies on the angle of attack in their derivations was utilised.

The usage of a porous medium model for incorporating the interaction of fluid and net into a CFD solver comes with several drawbacks which will be presented in section 2. This leads to the proposition of a new coupling model which is the subject of this paper. The new model utilises a screen force model to calculate the forces on the net accurately and distributes their influence on the fluid using Lagrangian points. Section 3 introduces the governing equations and the applied numerical solver. Details about the net and hydrodynamic force model which are necessary for the further understanding of the proposed model are also presented. The derivation of the new coupling methodology can be found in section 4. In section 5, a discussion of the overall numerical model is presented, while section 6 is devoted to several validation cases of fixed net walls and cages in varying wave and current conditions. Conclusions arising from the previous sections are given in section 7.

2 Review of the porous medium approach for coupling net and fluid in CFD solvers

The porous medium model is considered as a surrogate sharing similar physical properties as the original interaction process, but it does not imply any physical connection. This is illustrated by the necessity of arbitrarily [12] defining the added mass coefficient, originating from the derivation of the volume- and Reynolds-averaged Navier-Stokes (VRANS) equations, or neglecting it [29]. The closure model for the VRANS equations is usually based on the Darcy-Forchheimer law and requires the predefinition of several coefficients which are dependent on fluid properties. Previous research [12, 40] neglected these dependencies and rather used the free coefficients for incorporating the disturbances of the net on the fluid. As pointed out by Chen and Christensen [12], it is challenging to incorporate all aspects of properties influencing the forces on a net into the calculation of these coefficients. Therefore, they defined them as normal and tangential constants throughout the porous medium. This leads to a zone of constant pressure loss rather than a thin sheet where the pressure drops immediately as in reality.

Another challenge of porous medium models occurs for net cages and deformed nets in general. In [11], the utilisation of a porous medium for these cases is investigated where the authors proposed defining zones of certain thickness around each macro element of the net. The resulting prism volumes represent a continuous porous medium. This procedure might be interpreted as a type of overset grid. Besides the high computational cost of generating and parallelising this generally three-dimensional grid, a more severe problem occurs in the case of deformed elements. As shown in Fig. 1, overlapping regions and gaps can occur at possible intersections of zones. So far, this issue has not been addressed.
In order to keep the validity of the porous medium model, a solution of this geometrical problem is sought in preparation of the current paper. The idea was based on defining a point cloud of certain distance to the net elements. A Delaunay triangulation was then applied

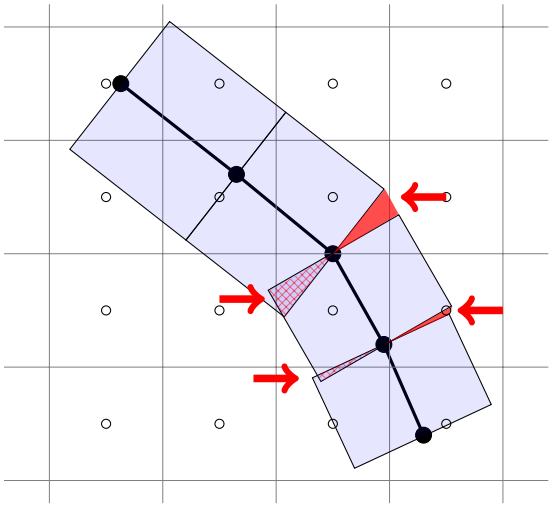

Figure 1: Two-dimensional illustration of the challenges in constructing a discrete porous zone (blue shaded) around a net wall (thick black lines and points) as proposed in [11]. Overlapping regions are indicated in hatched red; Holes are indicated as red triangles.

for generating a continuous volume enclosing the original net, and a level set function was defined around the volume and used for calculating normal vectors. These could be utilised for the calculation of the resistance coefficients in arbitrary directions. As a consequence of the Delaunay triangulation, concave shapes which occur inside a circular cage cannot be handled properly. This demonstrates the non-applicability of this approach in practice. Further, the triangulation process is computationally very demanding and challenging to parallelise. The correct assignment of the porous media closure terms to the surrounding grid cells is another unsolved problem arising in porous medium models, i.e. how to determine the portion of a particular porous zone in a fluid cell.

These drawbacks of the porous medium approach indicate theoretical, physical and computational limitations, and the necessity for an alternative coupling model arises. Therefore, a new coupling model based on Lagrangian-Eulerian considerations is proposed in this paper. The new approach avoids demanding volume handling and is straightforward to be parallelised. It also incorporates more advanced hydrodynamic force calculations. This increases the actual physical information contained in the coupling process and, eventually, improves numerical tools for modelling this type of fluid-structure interaction.

3 Numerical model

3.1 Fluid model

The basis of the new development in this paper is the open-source CFD solver REEF3D [7, 8]. It solves the continuity and Reynolds-averaged Navier-Stokes (RANS) equations for

incompressible fluids which can be written in indices notation as

$$\frac{\partial u_i}{\partial x_i} = 0, \tag{1}$$

$$\frac{\partial u_i}{\partial t} + u_j \frac{\partial u_i}{\partial x_j} = -\frac{1}{\rho}\frac{\partial p}{\partial x_i} + \frac{\partial}{\partial x_j}\left(\nu\left(\frac{\partial u_i}{\partial x_j} + \frac{\partial u_j}{\partial x_i}\right)\right) + g_i, \tag{2}$$

with u_i the velocity components, p representing the pressure and g_i the gravity acceleration vector. The kinematic viscosity ν contains the turbulent viscosity which is calculated from turbulent properties using the Boussinesq approximation. If the free surface is considered, the density ρ and ν have to be distinguished in the two phases. Following the ideas in [9], the material properties at any location are defined as

$$\rho = \rho_w H(\phi) + \rho_a(1 - H(\phi)), \tag{3}$$

$$\nu = \nu_w H(\phi) + \nu_a(1 - H(\phi)), \tag{4}$$

with w indicating water and a air properties. ϕ defines a signed distance function introduced below. H presents a smoothed Heaviside step function chosen as

$$H(\phi) = \begin{cases} 0 & \text{if } \phi < -\epsilon \\ \frac{1}{2}\left(1 + \frac{\phi}{\epsilon} + \frac{1}{\pi} sin(\frac{\pi\phi}{\epsilon})\right) & \text{if } |\phi| \leq \epsilon \\ 1 & \text{if } \phi > \epsilon, \end{cases} \tag{5}$$

with $\epsilon = 2.1\Delta x$ and Δx the characteristic length scale of the discrete domain.

The location of the free water surface is represented implicitly by the zero level set of a smooth signed distance function ϕ [28]. The gradients of ϕ satisfy the Eikonal equation $|\nabla\phi| = 1$. The motion of the free surface is captured by solving the linear advection equation with the fluid velocities u_i convecting ϕ. A reinitialisation step has to be incorporated after each time step to preserve the Eikonal equation. In the given framework, the reinitialization equation of Sussman et al. [35] is solved with an artificial time-stepping for this purpose.

Numerical solutions of the equations are sought using finite difference methods on rectilinear grids. The coupling of pressure and velocity during the solution of the system (1) and (2) is ensured by staggering the locations of velocity and pressure information. A fifth-order accurate weighted essentially non-oscillatory (WENO) scheme [16, 17] adapted to non-uniform cell sizes is applied to convection terms. Diffusion terms are discretised using second-order accurate central finite differences. The solution process follows the projection method for incompressible flows of Chorin [13]. In a first step, the momentum equations without pressure gradients are solved for predicting the velocities $u_i^{(*)}$:

$$\frac{u_i^{(*)} - u_i^{(n)}}{\Delta t} = -u_j \frac{\partial u_i}{\partial x_j} + \frac{\partial}{\partial x_j}\left(\nu \cdot \left(\frac{\partial u_i}{\partial x_j} + \frac{\partial u_j}{\partial x_i}\right)\right) + g_i. \tag{6}$$

In this study, the third-order accurate TVD Runge-Kutta scheme [34]

$$\begin{aligned} u_i^{(1)} &= u_i^{(n)} + \Delta t\ \mathbf{L}\left(u_i^{(n)}\right), \\ u_i^{(2)} &= \frac{3}{4}u_i^{(n)} + \frac{1}{4}u_i^{(1)} + \frac{1}{4}\Delta t\ \mathbf{L}\left(u_i^{(1)}\right), \\ u_i^{(*)} &= \frac{1}{3}u_i^{(n)} + \frac{2}{3}u_i^{(2)} + \frac{2}{3}\Delta t\ \mathbf{L}\left(u_i^{(2)}\right), \end{aligned} \tag{7}$$

is applied for solving Eq. (6) in time. In a second step, a Poisson equation is defined for the pressure:

$$\frac{\partial}{\partial x_i}\left(\frac{1}{\rho}\frac{\partial p^{(n+1)}}{\partial x_i}\right) = \frac{1}{\Delta t}\frac{\partial u_i^{(*)}}{\partial x_i}. \tag{8}$$

It is solved using the fully parallelized BiCGStab solver with geometric multigrid preconditioning of the HYPRE library [37]. Adaptive time stepping controls the time steps according to the required CFL condition. A divergence free velocity field is finally found by correcting the predicted velocities in accordance with

$$u_i^{(n+1)} = u_i^{(*)} - \frac{\Delta t}{\rho}\frac{\partial p^{(n+1)}}{\partial x_i}. \tag{9}$$

An n-halo domain decomposition strategy is implemented in the CFD solver. Here, the domain is split into several subdomains, and data is transferred to neighbouring subdomains using several layers of ghost cells. Convection term containing equations require three layers due to the application of the fifth-order accurate WENO scheme. Otherwise, one layer is sufficient because at most second-order accurate spatial discretization schemes are applied. High-performance computation is enabled by using the message passing interface (MPI) for inter-processor communication.

3.2 Net model

The development of the quasi-static net model implemented in the fluid solver is thoroughly described in [26]. The initialisation process of the net model is applied in this study to calculate hydrodynamic forces on the fixed net. Thus, a discrete representation of the net is assumed. It consists of several knots connected with elastic bars. Each macro element is defined by four knots and four bars. It can represent several meshes depending on the solidity of the net. Assuming square meshes, the solidity S can be approximated as in [15]:

$$S = \frac{2d_t}{l_t} - \left(\frac{d_t}{l_t}\right)^2, \tag{10}$$

with d_t the diameter and l_t the length of each twine. An example of a discrete net is shown in Fig. 2.

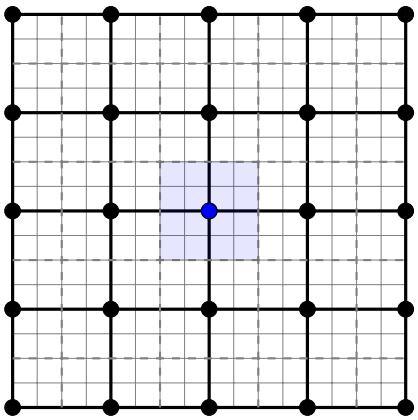

Figure 2: Illustration of a discrete representation of a physical net (thin lines): black dots represent knots, thick black lines represent bars. Dashed lines show the distribution of the screens for the force calculation. For example, the blue areas correspond to the blue knot.

3.3 Hydrodynamic force model

In contrast to previous research on this subject, the proposed model includes the dependency on all important properties for calculating hydrodynamic forces. Following the screen force model of Kristiansen and Faltinsen [20], the net area is distributed on adjoint knots as indicated in Fig. 2. Thus, the contributions of up to four panel parts (screens) add up to the hydrodynamic forces corresponding to a single knot. The surface integral of each screen is approximated by a second-order accurate quadrature rule using its geometrical centre as the integration point. On each screen, two force vectors $\vec{F}_D$ and $\vec{F}_L$ are defined in the normal and tangential direction to the inflow velocity vector, which can be identified as drag and lift force directions $\vec{n}_d$ and $\vec{n}_l$:

$$\vec{F}_D = \frac{\rho}{2} C_D A u_{rel}^2 \vec{n}_d, \tag{11}$$

$$\vec{F}_L = \frac{\rho}{2} C_L A u_{rel}^2 \vec{n}_l, . \tag{12}$$

Here, A is the area of the screen given as

$$A = \frac{l_1 l_2}{4} \cdot |\vec{b}_1 \times \vec{b}_2|, \tag{13}$$

with indices 1 and 2 referring to the two bars spanning the area and $\vec{b}$ the unit bar vectors. Further, u_{rel} represents the magnitude of the relative velocity vector $\vec{u}_{rel}$ between the inflow velocity u_∞ and the velocity of the panel which is zero in this paper. The two necessary directions are determined as follows

$$\vec{n}_d = \frac{\vec{u}_{rel}}{|\vec{u}_{rel}|}, \tag{14}$$

$$\vec{n}_l = \frac{(\vec{u}_{rel} \times \vec{n}_s) \times \vec{n}_s}{|(\vec{u}_{rel} \times \vec{n}_s) \times \vec{n}_s|}, \tag{15}$$

where $\vec{n}_s$ is the unit normal vector of the screen pointing in the same direction as $\vec{u}_{rel}$. The unknown force coefficients C_D and C_L are calculated from a truncated Fourier series expanded for their dependency on the angle of attack α

$$C_D(\alpha) = C_{D,0} \sum_{n=1}^{\infty} a_{2n-1} \cos\left((2n-1)\alpha\right), \tag{16}$$

$$C_L(\alpha) = C_{L,\frac{\pi}{4}} \sum_{n=1}^{\infty} b_{2n} \cos\left(2n\alpha\right). \tag{17}$$

In [20], details about the calculation of the constants $C_{D,0}$ in Eq. (16) and $C_{L,\frac{\pi}{4}}$ in Eq. (17) are given. However, they kept the determination of the Fourier coefficients a and b open for discussion. In accordance with the idea of Yao et al. [38], optimum coefficients are found by fitting them to experimental data. Currently, the available amount of measurements for drag and lift forces on nets is rather small and specific for nets with low solidity. High solidity measurements as provided in [4] are important contributions for future adjustments, in particular with regards to bio-fouled nets.

The chosen fitting data is taken from the measurements and data provided by Patursson et al. [29]. Additionally, data from Zhan et al. [39] is included for the drag force prediction. In total, the data set spans solidities between 0.128 and 0.317 and inflow velocities between 0.159 m/s and 1.0 m/s. It also includes the whole range of possible angles of attack ($0° - 90°$). Non-linear fitting is accomplished using the downhill simplex method [27] with constraints to keep the results physically bounded and fulfil the condition $C_D(\alpha = 0) = C_{D,0}$. Solidity, twine diameter, inflow velocity and angle of attack are defined as fitting parameters. The optimum is sought and compared for up to four Fourier coefficients for C_D and three Fourier coefficients for C_L. Tab. 1 shows the resulting coefficients for the best fit. The mean absolute percentage error (MAPE) for the C_D fitting problem is 17.3%, 8.5% and 35.1% for the two data sets in [29] and the data in [39] if three coefficients are used. However, the fit would be just slightly worse if just two coefficients, as proposed in [20], are used. For C_L, the best MAPE is 20.9% and 14.2% for the data in [29] if the series is truncated after two coefficients. As indicated in [38], a better fit can be achieved if b_2 is set larger than one. Thus, the applied Fourier series is

$$C_D(\alpha) = C_{D,0} \cdot \left[0.9725 \cos\left(\alpha\right) + 0.0139 \cos\left(3\alpha\right) + 0.0136 \cos\left(5\alpha\right)\right], \tag{18}$$

$$C_L(\alpha) = C_{L,\frac{\pi}{4}} \cdot \left[1.2291 \cos\left(2\alpha\right) + 0.1116 \cos\left(4\alpha\right)\right]. \tag{19}$$

Table 1: Calculated Fourier coefficients using a multidimensional optimisation method with bounded constraints.

a_1	a_3	a_5	a_7	b_2	b_4	b_6
0.9725	0.0139	0.0136	0.0	1.2291	0.1116	0.0

4 New Lagrangian-Eulerian coupling algorithm

A new methodology for modelling the interaction of net and fluid is proposed in this section. This method aims to provide better physical representation, higher modelling flexibility and

lower computational cost in comparison to porous media representations. It is based on a Lagrangian-Eulerian approach as it is originally developed for impermeable membranes [30] and applied to e.g. parachute modelling [3]. In section 4.1, a Lagrangian model to represent the net is described, followed by the coupling process to the fluid in section 4.2. A general problem from this coupling is the modified velocity near the net. In contrast to previous research, this paper proposes a physical correction for this problem in section 4.3. The resulting model creates a free parameter which is used for adapting the correct velocity reduction behind the net. Section 4.4 is devoted to provide details about it.

4.1 Lagrangian representation of the net

A Lagrangian representation of the net is found as a first step. In order to keep flexibility, no assumption about the ratio between the Eulerian cell size of the fluid and the macro element size representing the net is stated. The disturbance of the fluid by the net should be nearly equally distributed over the area of the net. Hence, the distance between Lagrangian points is connected to the cell size of the surrounding Eulerian grid. In case the grid is rather coarse, the numerical representation of the net as macro elements is sufficient. However, the macro elements should be refined if the grid is refined. The most efficient way of automating this process is to divide the net elements into triangles and compare their average length with a reference cell size (see Fig. 3). If the length exceeds the reference length, the triangle is split into four smaller triangles using the centre of each side as an additional vertex. Further iterations are executed until the criterium is fulfilled. The Lagrangian points are then set in the geometrical centre of each triangle.

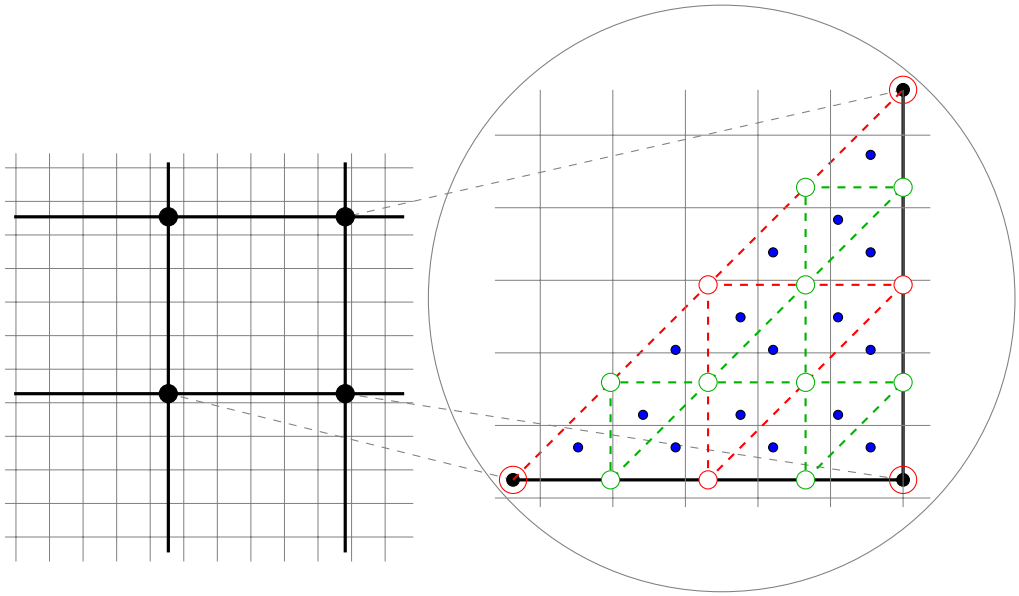

Figure 3: Illustration of the procedure for obtaining a Lagrangian representation of one half of a net element (thick lines and points) in a Eulerian fluid domain (thin grey lines). Red lines and dots indicate the triangles after the first triangulation loop, green lines and dots result from the second loop. The resulting Lagrangian points are shown in blue.

4.2 Coupling process

A coupling condition can be enforced starting from the Eulerian grid for the fluid and the Lagrangian points representing the net. Conservation of momentum is assumed for any control volume enclosing the net. It results in the condition that the energy transfer from the fluid to the net corresponds to the loss of the fluid momentum due to the disturbance of the net. This momentum loss can be physically identified as a pressure jump over an infinitesimally small distance through the net. Looking into the procedure of the projection method from above, a modification of Eq. (8) can incorporate this change. It leads to the updated Poisson equation

$$\frac{\partial}{\partial x_i}\left(\frac{1}{\rho}\frac{\partial p^{(n+1)}}{\partial x_i}\right) = \frac{1}{\Delta t}\frac{\partial}{\partial x_i}\left(u_i^{(*)} - F_i\right), \tag{20}$$

and the new velocity correction step

$$u_i^{(n+1)} = u_i^{(*)} - F_i - \frac{\Delta t}{\rho}\frac{\partial p^{(n+1)}}{\partial x_i}, \tag{21}$$

with $F_i = F(\vec{x}_e)_i$ being one component of the momentum loss vector due to the presence of the net at point $\vec{x}_e$ of the Eulerian grid. Following the idea of Peskin [30], it can be calculated from

$$F(\vec{x}_e)_i = \sum_{l=1}^{L} D(\vec{x}_e, \vec{x}_l) \cdot f(\vec{x}_l)_i, \tag{22}$$

where $f(\vec{x}_l)_i$ is the i-th component of the hydrodynamic screen force vector at the Lagrangian point $\vec{x}_l$ and L is the number of Lagrangian points within a defined Kernel D around $\vec{x}_e$. A modification of Eq. (22) is proposed to have a more flexible choice for the diameter of the kernel. For this purpose, $F(\vec{x}_e)_i$ is calculated using the inverse distance weighting

$$F(\vec{x}_e)_i = \frac{\sum_{l=1}^{L} w_{e,l} \cdot f(\vec{x}_l)_i}{\sum_{l=1}^{L} w_{e,l}}, \tag{23}$$

with the dimensionless weights

$$w_{e,l} = \frac{1}{|\vec{x}_e - \vec{x}_l|^2}. \tag{24}$$

The chosen distribution of F over a certain volume of the fluid grid is illustrated in 2D in Fig. 4. Special attention has to be given to the staggered grid arrangement. For example, the x-component of the force is distributed only on the grid of the x-velocity component.

Finally, the forces at each Lagrangian point $\vec{f}(\vec{x}_l)$ in the principal direction of the Eulerian grid are calculated. By comparing to the described screen forces in Eq. (11) and Eq. (12), they can be expressed as the integrand of the surface integral:

$$f(\vec{x}_l)_i = F_{D,i}(\vec{x}_l) + F_{L,i}(\vec{x}_l) = \frac{\rho}{2} u_{rel}^2 \cdot \left(C_D n_{d,i} + C_L n_{l,i}\right). \tag{25}$$

A dimensional analysis of Eq. (23), Eq. (25) and Eq. (20) shows equality only if $\vec{f}(\vec{x}_l)$ is divided by a length. The necessary parameter κ with dimension $[1/m]$ arises from the transition from a surface force to a volume force and is the diameter of the influence sphere of each Lagrangian point. In subsection 4.4, κ is determined to represent the correct velocity reduction behind the net. The momentum loss vector is finally calculated as

$$F(\vec{x}_e)_i = \frac{1}{\kappa} \cdot \frac{\sum_{l=1}^{L} w_{e,l} \cdot f(\vec{x}_l)_i}{\sum_{l=1}^{L} w_{e,l}}. \tag{26}$$

It is noticed that the new coupling algorithm theoretically does not fulfil the law of momentum conservation because the net forces are calculated on the original macro elements but the disturbances on the fluid are determined from a usually finer triangulated surface. This choice is made for efficiency reasons and motivated by the valid assumption of small velocity changes within one net screen. It is in particular reasonable if in both steps the velocities are interpolated using the same inverse distance weighting algorithm.

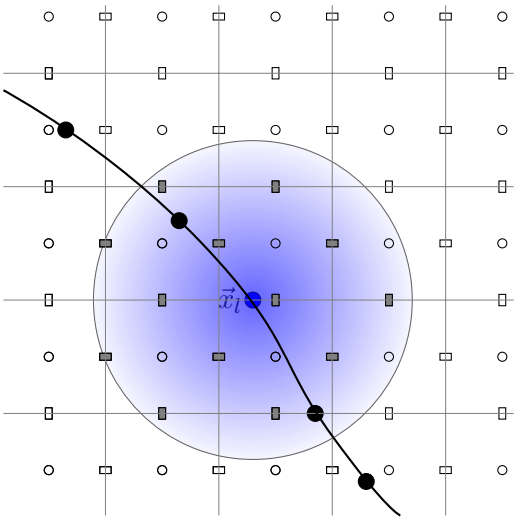

Figure 4: Distribution of the force $\vec{F}(\vec{x}_l)$ of point $\vec{x}_l$ (blue) on the Eulerian grid points (white dots and rectangles). Blue shading illustrates inverse weighting for surrounding fluid points. The influenced velocity nodes are coloured in grey.

4.3 Improving the velocity prediction

A challenge arising from the numerical representation of the net within the fluid domain is the disturbed velocity field around the net. As shown in Fig. 5, the velocity at the net differs from the undisturbed inflow velocity due to the discrete interpolation (Eq. (23)). In previous research [29], this was overcome by fitting the porous medium coefficients numerically which implicitly respects this difference in velocity. In the current model, the force coefficients are determined based on the assumption of undisturbed velocities in front of the net in accordance with most force models. Thus, a relationship between the numerically interpolated velocity at the net and the undisturbed inflow velocity has to be derived.

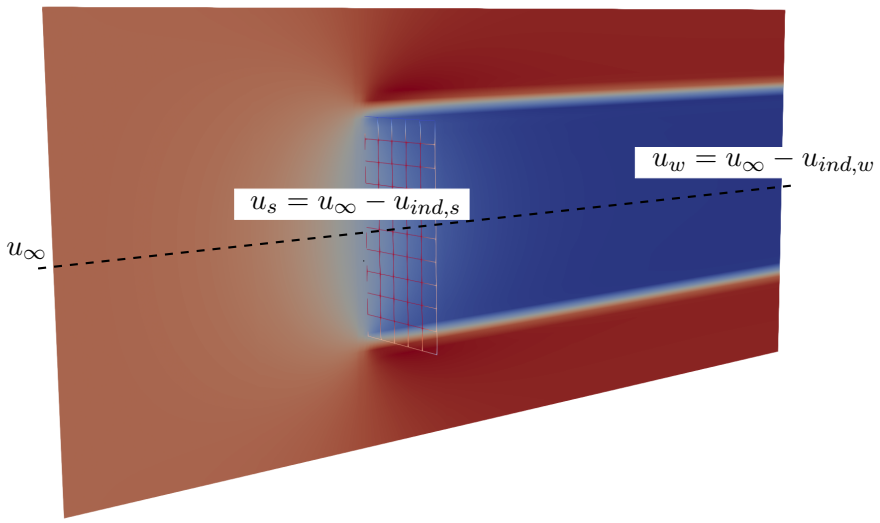

Figure 5: Illustration of velocity definitions in front and behind the net. Cross section shows the x-velocity distribution with velocity reduction behind the net.

One possibility is the approach of Løland [25] which is based on the linearised turbulent wake equations of Schlichting [33]. A more proven concept is based on Froude's momentum theory [10]. In the research area of hydrodynamics, it is applied to include the discrete disturbance of a propeller disk in a fluid domain. Here, the balance of momentum before and behind an infinitesimally thin rotating screen has to be calculated. In the following, this approach is elaborated for net applications. Besides the assumptions valid for potential flows, it is assumed that the induced velocities from the screen $u_{ind,s}$ and in the wake $u_{ind,w}$ are much smaller than the inflow velocity u_∞ and no rotational velocities are induced (see Fig. 5 for definitions). Then, two Bernoulli equations can be stated:

$$p_\infty + \frac{\rho}{2} u_\infty^2 = p_{s,1} + \frac{\rho}{2}(u_\infty - u_{ind,s})^2, \tag{27}$$

$$p_{s,2} + \frac{\rho}{2}(u_\infty - u_{ind,s})^2 = p_w + \frac{\rho}{2}(u_\infty - u_{ind,w})^2. \tag{28}$$

Eq. (27) is valid in front of the screen and Eq. (28) describes the fluid behind the screen. By combining these equations, the pressure jump at the screen is defined as

$$\Delta p = p_{s,2} - p_{s,1} = p_w - p_\infty + \rho\, u_{ind,w} \cdot \left(-u_\infty + \frac{u_{ind,w}}{2}\right). \tag{29}$$

It can be assumed that $p_w = p_\infty$ if start and end point are far away from the disturbance. Thus, Eq. (29) expresses the pressure jump in terms of inflow and induced velocities. Linearisation of the equation yields

$$\Delta p \approx -\rho\, u_{ind,w}\, u_\infty. \tag{30}$$

In addition, Eq. (27) can be used to approximate the pressure jump in front of the screen. The linearised expression is

$$p_{s,1} - p_\infty = \rho\, u_\infty\, u_{ind,s}. \tag{31}$$

Froude's hypothesis arises from Eq. (31) if the assumption is made that half of the pressure jump is in front and the other half behind the screen,

$$u_{ind,w} = 2u_{ind,s}, \tag{32}$$

i.e. the velocity at the screen is half the velocity between inflow and wake velocity (see Fig. 6). By inserting this result in Eq. (30) and using the definition of the screen velocity, it yields a new formula for u_s:

$$u_s = u_\infty - \frac{\Delta p}{2\rho u_\infty}. \tag{33}$$

The pressure jump Δp is due to the disturbance forces from Eq. (25) normal to the screen. Using the fluid velocity at the screen and the inflow velocity for the coefficient calculation, the jump can be expressed as

$$\Delta p = \frac{\rho}{2} C_D(u_\infty) u_s^2. \tag{34}$$

In combination with Eq. (33), the inflow velocity can finally be approximated from the known screen velocity as

$$u_\infty = \frac{C_D(u_\infty)}{2 \cdot \left(\sqrt{1 + C_D(u_\infty)} - 1\right)} \cdot u_s. \tag{35}$$

In the later validation process, Eq. (35) is solved using the Newton-Raphson method with $u_\infty = u_s$ as an initial guess.

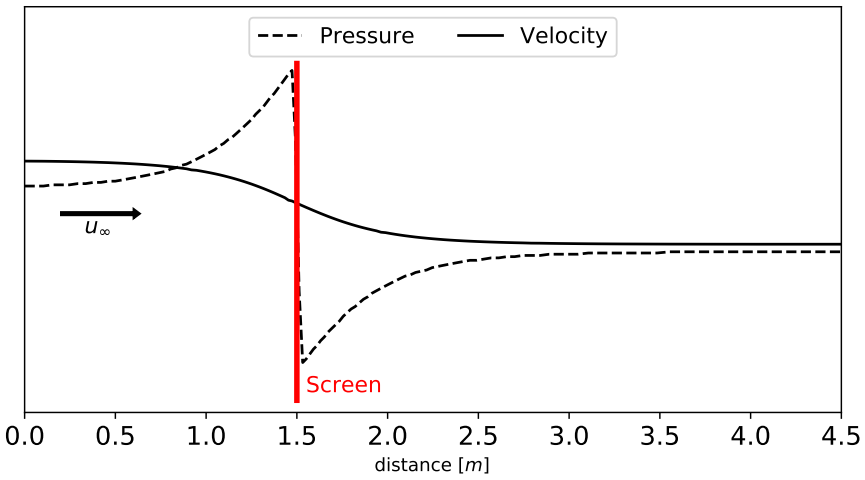

Figure 6: Illustration of velocity and pressure distribution in front and behind the net.

4.4 Estimating the velocity reduction through the net

The derivation of the new coupling algorithm in section 4.2 leads to a free parameter κ to fulfil dimensional equality. It arises numerically with the transition from the hydrodynamic surface

force at the screens to a volume force representation in the Eulerian grid. The parameter corresponds physically to the influence range of the net disturbance on the fluid and is linked to the deceleration of the flow behind the net. In porous medium models, the parameter was determined implicitly through coupling it to the resistance coefficients. Thus, a single fitting was used for both, the velocity reduction and the force calculation. In the new proposed model, these two effects can be investigated separately through the introduction of the velocity reduction correction in the previous section.

A physical determination of κ for approximating the correct velocity reduction behind nets is preferable. However, the available measurements are not sufficient for conclusions at this stage of research. Rudi et al. [32] performed measurements of the velocity reduction behind vertical net sheets, but the data is not publicly available. Patursson et al. [29] measured the same effect but only for a single net solidity. Their results indicate that the dependency of the reduction on the inflow velocity is marginal. The dependency on the angle of attack is also less significant for angles larger than 30°. For smaller angles, the frame of the net wall modifies the solidity of the actual sheet, and the reduction increases disproportionally. The highest influence is expected due to changing net solidity, but more numerical and physical experiments have to be conducted to find correlations. In general, the velocity reduction is documented using the velocity reduction factor U_r which is given as

$$U_r = 1.0 - \frac{u_w}{u_\infty}. \tag{36}$$

As pointed out by Løland [25], this parameter is very sensitive with respect to the measured wake velocity. This further complicates the accurate prediction of the velocity reduction numerically. As a starting point and unless stated otherwise, the validation cases are computed using $\kappa = 0.07$ which is determined from comparing U_r with the data in [29].

5 Summary of the proposed model

A flowchart illustrating the proposed Lagrangian-Eulerian fluid-structure interaction (FSI) algorithm is provided in Fig. 7. Three steps are executed in addition to the original fluid solution algorithm [8]. Each time step starts with the calculation of the free surface using the level set method, and material properties are updated as given in Eq. (3) - Eq. (5). These steps can be omitted in a one-phase simulation. The projection method initially performs the predictor step (Eq. (6)) for the velocities. The hydrodynamic loads on the discrete net structure are computed using Eq. (11) and Eq. (12). In case of a moving net algorithm, the net is then advanced in time. Based on the new position of the net, the position of the Lagrangian points describing the net in the fluid are corrected, and disturbances are distributed on the Eulerian grid by applying Eq. (23). Finally, the modified Poisson equation (20) is solved, and the velocity field is corrected to be divergence-free.

The choice of the kernel radius remains from the previous sections. In the given implementation, it has a minor influence on the results as long as the recommended distance between the Lagrangian points is used. In case of a ghost cell approach as described above, the given number of additional cell layers needed for solving the RANS equations is adequate to store all information needed for the local kernel interpolations. Thus, the only inter-processor communication is the distribution of the disturbance field before the solution of the Poisson equation. This reduces the computational costs significantly and simplifies the parallelisation process.

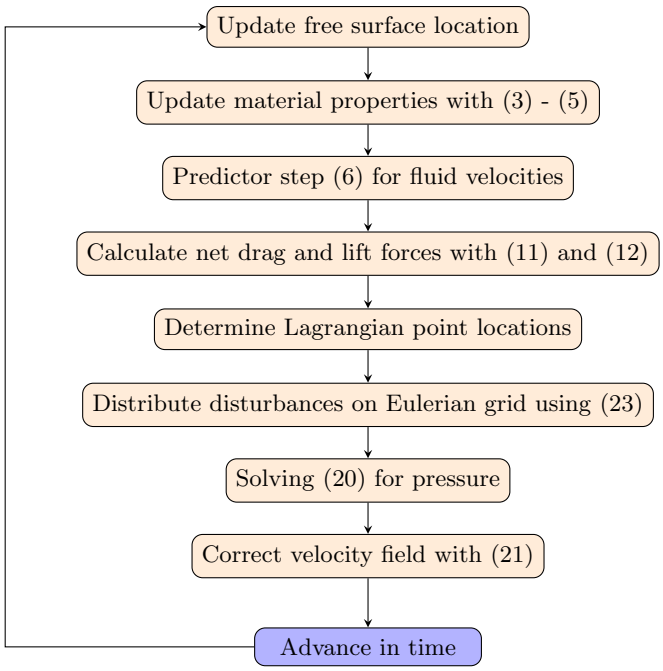

Figure 7: Flowchart of the presented Lagrangian-Eulerian FSI algorithm.

Regarding turbulence modelling, the proposed model consisting of macro elements prevents the resolution of turbulence interactions between net and fluid. Chen and Christensen [12] hypothesised that vortices smaller than the mesh size convect freely through the net, whereas larger vortices are split. Simultaneously, the wake of the individual twines and knots is characterised by separated vortices and strong interaction between them. It is in the interest of the research community to investigate these effects more thoroughly [23] because the turbulence influences the flow transported to the back part of the net cage and the fish inside the cage. The most promising approach for incorporating these effects into a RANS model is their expression as additional generation and dissipation terms in the equation for the turbulent kinetic energy (TKE). This requires an extensive study on TKE changes due to inflow turbulence intensity, angles of attack and net geometry, and is not restricted only to numerical investigations since experimental validation data has to be available as well. It exceeds the scope of this paper to include such investigations. Instead, the indications in [12], that the turbulence might have minor effects on integral quantities like the total load on a net in practice, are taken into account. Further, the incorporation of experimental data into the derivation of the numerical model presumably includes the influence of turbulent effects for the loads. Hence, turbulence modelling is neglected in the following validation section.

6 Validation process

Results from the new solver are compared to available experimental data for total forces on fixed net sheets and cages. The numerical forces on the net are determined by integrating the discrete forces from Eq. (11) and Eq. (12) over the whole net area. The quantitative validation of the results is performed by calculating the percent deviation between the numerical result

Φ_{num} and the measured value Φ_{exp}:

$$\text{Deviation} = \frac{\Phi_{\text{exp}} - \Phi_{\text{num}}}{\Phi_{\text{exp}}} \cdot 100. \tag{37}$$

The sign of the deviation is kept for analysing the over- and under-predictions of the model.

6.1 Forces and velocity reduction for a fixed net panel in steady current flow

A fixed net panel is compared to the experimental data of Patursson et al. [29] in a steady current of different velocities and under several angles of attack α. Here, the drag and lift force coefficients and the velocity reduction factor behind the net as given in Eq. (36) are considered. For the latter, the wake velocity is measured 2.5 m behind the net. The comparability of the velocity at that specific point is not valid because of the continuous numerical representation of the net in the fluid domain. Therefore, velocity probes are arranged in the form of a disc around the measured point and the average value is compared with that from the experiment. This should provide a better impression of the numerical accuracy because it takes the discrete approach of macro elements into account.

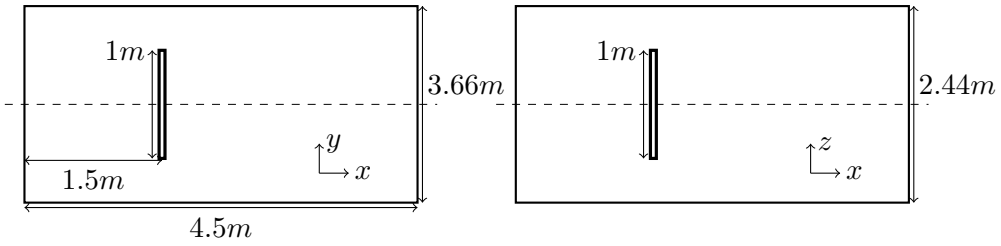

Figure 8: Computational domain for the simulation of a fixed net panel in steady current flow. Top view is shown on the left, side view is shown on the right.

The net is fixed in a frame of 1.0 m × 1.0 m and has a solidity of 0.184. The frame is not considered in this study due to missing geometrical data. This is in accordance with previous calculations [12, 29]. Four different angles of attack, i.e. $\alpha = 15°, 30°, 45°, 90°$ and four different inflow velocities between 0.125 m/s and 0.75 m/s are investigated. Here, 90° corresponds to perpendicular inflow conditions. The computational domain is 4.5 m × 3.66 m × 2.44 m, and the geometrical centre of the net is kept at (1.5 m, 1.83 m, 1.22 m) for all angles of attack (see also Fig. 8).

A spatial convergence test is conducted for the configuration $\alpha = 45°$ and $u_\infty = 0.5$ m/s. The validation process as given in [31] is applied to check convergence. For this purpose, three grids with 0.423 million, 1.22 million and 3.45 million cells with a gradual refinement towards the net are considered. The deviation for C_D and C_L are oscillatory converging, and the deviation of U_r is monotonically converging. As can be seen in Tab. 2, the differences between the results on the different grids are generally small. Therefore, it is decided to utilise the coarsest grid for the following computations. Temporal convergence is not investigated because the simulations result in steady-state conditions.

A slice of the domain through the middle plane is shown for $\alpha = 45°$ and 90° and $u_\infty =$ 0.5 m/s in Fig. 9. The wake of the net is visible and has approximately the same width as

Table 2: Convergence test for the fixed net wall in steady current flow. Table shows the deviations [%] for the drag and lift coefficients and the velocity reduction for the three different grids.

	Coarse	Medium	Fine
C_D	-6.48	-4.90	-6.41
C_L	-17.16	-14.52	-15.57
U_r	7.64	7.09	6.86

the net panel. The fluid is accelerated around the panel. As the angle of attack increases, the fluid slows down in front of the net which leads to a decreasing velocity at the net itself. Behind the net, a nearly steady velocity field can be observed for both angles of attack.

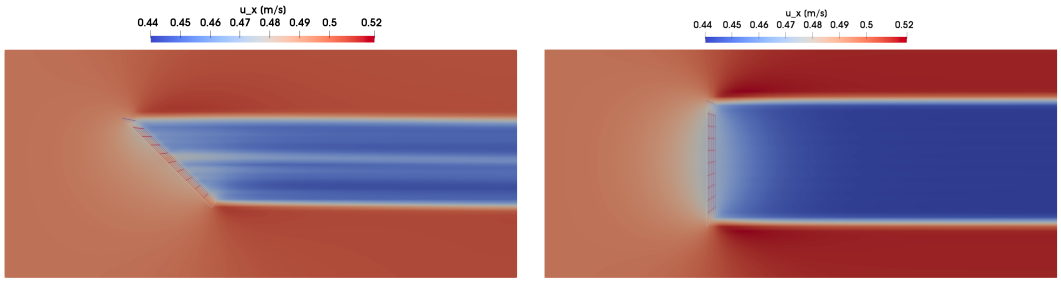

(a) $\alpha = 45°$. (b) $\alpha = 90°$.

Figure 9: Velocity field for the fixed net panel in steady current flow of $u_\infty = 0.5$ m/s.

Fig. 10 presents the numerical and experimental force coefficients for the different inflow velocities as a function of α. The computed drag coefficients (Fig. 10a) increase with decreasing inflow velocity and increasing angle of attack. This agrees qualitatively with the measurements. The predicted lift coefficients in Fig. 10b indicate maximum lift forces for $\alpha = 45°$. At larger angles of attack, the flow separates at the frame, and the lift forces reduce. In general, the lift forces are smaller than the drag forces. The velocity reduction behind the net is predicted well by the numerical model for $\alpha \geq 30°$ as can be seen in Fig. 10c. At smaller angles of attack, the deviations are as expected due to the choice of κ in section 4.4.

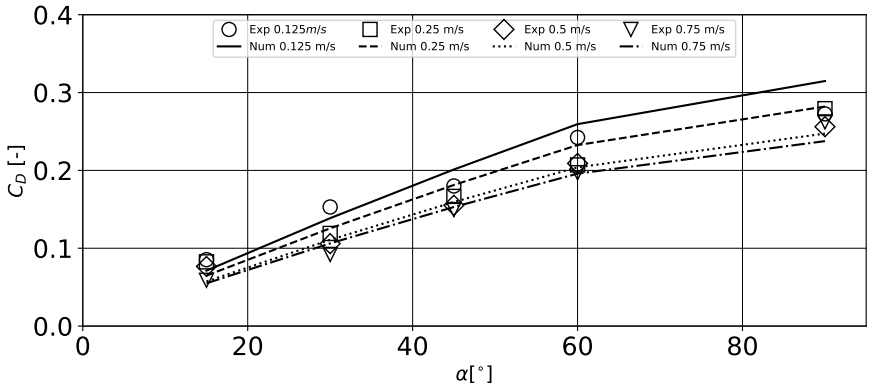

(a) Drag coefficient C_D.

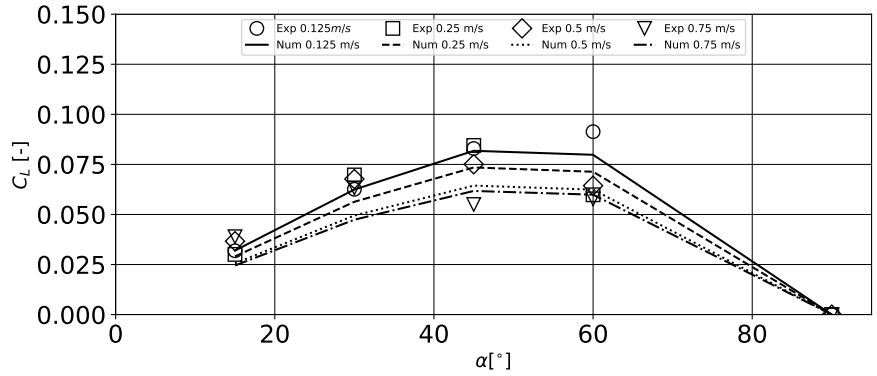

(b) Lift coefficient C_L.

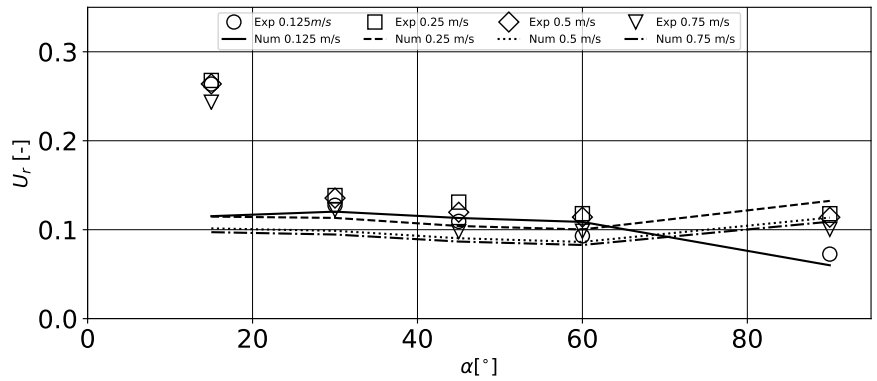

(c) Velocity reduction factor U_r.

Figure 10: Comparison of the numerical and experimental results for the fixed net panel in steady current flow.

The quantitative determination of the numerical results is presented in the Tabs. 3, 4 and 5. They present the deviations for all three properties at different fluid velocities and angles of attack. The maximum deviation in computing C_D is 25% for $\alpha = 15°$ which might be due to neglecting the influence of the frame. For larger angles, the maximum deviation is reduced to 15%. The L_2 norms of the deviation for the four different inflow velocities are

0.05, 0.04, 0.02 and 0.03, which indicates a good approximation of the model over the whole range of Reynolds numbers. Similar behaviour can be seen for C_L, where the L_2 norms of deviation are 0.01, 0.02, 0.02 and 0.02. However, the deviations are slightly larger than for the prediction for C_D with a maximum derivation of 27% for angles larger than 15°. These results describe an improvement over existing porous medium models [12] where deviations larger than 50% for C_L were reported. The maximum deviations for U_r are in a similar range as the deviations for C_L. The chosen constant κ seems to approximate the velocity reduction well over the considered range of angles of attack and Reynolds numbers. A tendency to better agreement to experiments can be observed for the larger angles of attack which coincides with the comments in section 4.4.

Table 3: Deviations [%] for the drag force coefficients between numerical simulation and experimental data of Patursson et al. [29].

α [°]	u_∞ [m/s]			
	0.125	0.25	0.5	0.75
15	16.53	21.40	25.09	6.49
30	9.39	−5.52	−4.60	−15.46
45	−11.76	−8.79	−2.71	−2.18
60	−7.06	−12.34	2.42	0.59
90	−15.47	−0.98	3.44	9.41

Table 4: Deviations [%] for the lift force coefficients between numerical simulation and experimental data of Patursson et al. [29].

α [°]	u_∞ [m/s]			
	0.125	0.25	0.5	0.75
15	−0.36	3.38	30.11	36.95
30	0.23	19.22	26.92	25.13
45	1.35	13.0	14.20	−12.33
60	12.63	−19.22	3.05	−3.61

Table 5: Deviations [%] for the velocity reduction factors between numerical simulation and experimental data of Patursson et al. [29].

α [°]	u_∞ [m/s]			
	0.125	0.25	0.5	0.75
15	56.32	57.16	61.55	60.04
30	5.63	18.18	27.16	22.65
45	−3.45	20.49	24.43	11.45
60	−16.87	15.05	24.45	15.75
90	−17.30	−12.20	0.34	−8.59

6.2 Drag forces on a fixed net panel in steady current flows

Further experiments on fixed net panels in current are presented by Zhan et al. [39]. Several net geometries with square meshes are investigated. This gives a better understanding of the proposed model for a variety of net solidities.

The net panel has a width of 1.3 m and a height of 0.7 m. Three angles of attack, i.e. $\alpha = 30°, 60°, 90°$ and four different inflow velocities between 0.25 m/s and 1.0 m/s are considered. The solidities of the net Sn are $0.128, 0.215$ and 0.223. The same computational domain, net position and grid as given in section 6.1 is used for the simulations.

The measurements are limited to drag forces. Fig. 11 presents the numerical and experimental drag force coefficients as a function of α. As observed before, the forces increase with decreasing inflow velocity and increasing angle of attack. The forces also rise with increasing solidity due to a growing number of twines or increase of twine diameter. The quantification of the results are presented in the Tabs. 6, 7 and 8. The largest deviations are calculated for $\alpha = 30°$ irrespective of the solidity and for all angles at $u_\infty = 0.25$ m/s, with a maximum deviation of 31%. A general trend of under- or over-prediction cannot be stated. This indicates the appropriate capturing of the physics by the proposed approach in the applied range of Reynolds numbers, angles of attack and net geometries. This impression is strengthened by considering the similarity of the L_2 norms of the deviation, which are 0.12, 0.09 and 0.10.

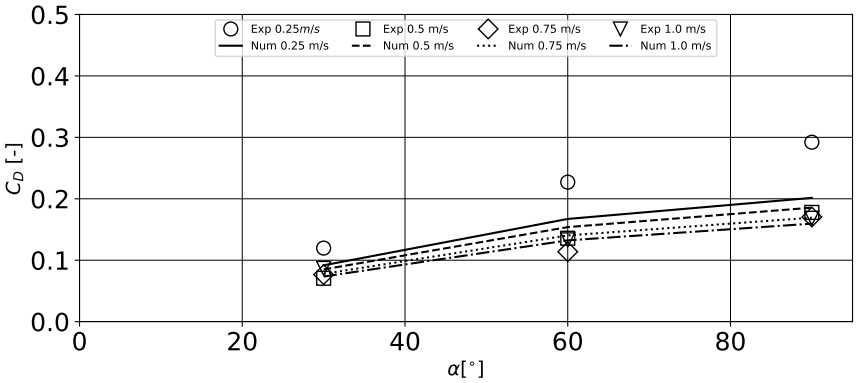

(a) $Sn = 0.128$.

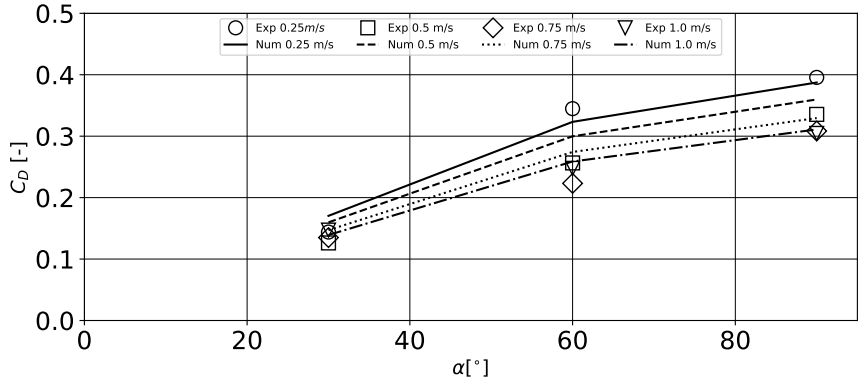

(b) $Sn = 0.215$.

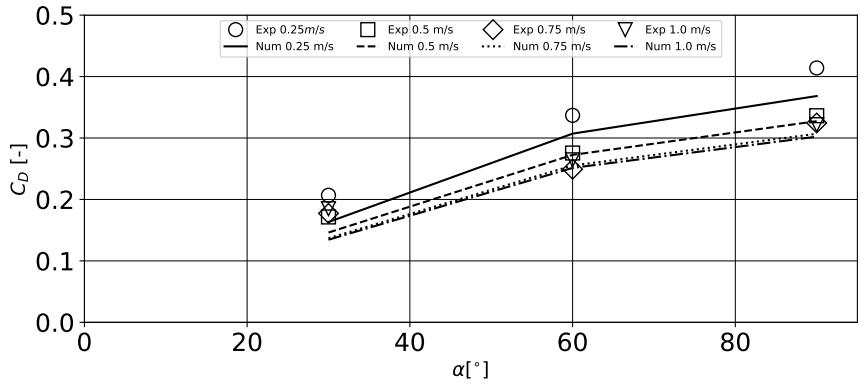

(c) $Sn = 0.223$.

Figure 11: Comparison of numerical and experimental drag coefficients for the fixed net panel in steady current flow.

Table 6: Deviations [%] for the drag force coefficients between numerical simulation and experimental data of Zhan et al. [39] for a net wall with $Sn = 0.128$.

α [°]	u_∞ [m/s]			
	0.25	0.5	0.75	1.0
30	23.40	−20.32	−1.57	15.35
60	26.39	−13.35	−23.32	0.66
90	31.02	−4.33	0.67	5.25

Table 7: Deviations [%] for the drag force coefficients between numerical simulation and experimental data of Zhan et al. [39] for a net wall with $Sn = 0.215$.

α [°]	u_∞ [m/s]			
	0.25	0.5	0.75	1.0
30	−18.34	−26.54	22.81	5.43
60	6.23	−16.91	−22.91	−4.49
90	2.10	−7.24	−6.83	−2.11

Table 8: Deviations [%] for the drag force coefficients between numerical simulation and experimental data of Zhan et al. [39] for a net wall with $Sn = 0.223$.

α [°]	u_∞ [m/s]			
	0.25	0.5	0.75	1.0
30	21.06	14.77	22.81	27.29
60	8.84	1.10	−2.43	4.97
90	11.04	2.64	5.43	6.06

6.3 Drag forces on a fixed net cage in steady current flows

A validation case with more complicated geometry is conducted in this section. In [39], the drag forces on fully submerged fixed circular net structures are measured for different inflow velocities and net geometries. The cage has a height of 0.7 m and a diameter of 0.414 m. The inflow velocities vary from 0.25 m/s to 1.0 m/s, and solidities of $0.128, 0.215$ and 0.223 are considered. The dimensions of the computational domain are illustrated in Fig. 12.

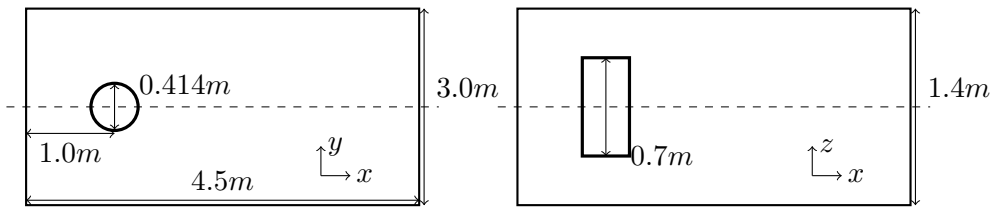

Figure 12: Computational domain for the simulation of a fixed net cage in steady current flow. The top view is shown on the left, the side view is shown on the right.

The predicted drag forces are compared to the experimental results in Fig. 13 and Tab. 9. In the experiments, the forces increase with the solidity and inflow velocity. In contrast, the numerical model computes slightly larger drag forces for $Sn = 0.215$ than for $Sn = 0.223$. The difference in solidity between the two nets seems to be small. However, the net with $Sn = 0.215$ contains meshes with half the length and half the diameter compared to the net with $Sn = 0.223$. Thus, the interaction between the twines increases for the net with $Sn = 0.215$. This effect is apparently not captured well by the screen force model because the deviations to the experiments are the largest for this net (up to 23% in deviation). The other net configurations are modelled within a range of a 20% deviation band, and the L_2 norms of deviation are 1.94 N and 3.15 N. This indicates a good capturing of the physics for the investigated range of inflow velocities and improvement over the results reported in [12].

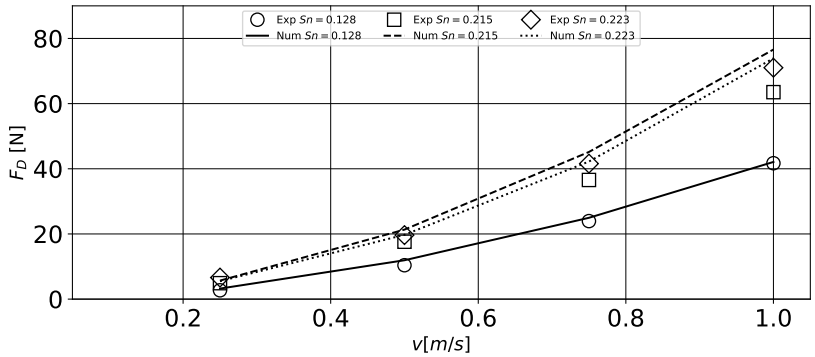

Figure 13: Comparison of the numerical and experimental drag forces on fixed net cage in steady current flow.

Table 9: Deviations [%] for the drag forces between numerical simulation and experimental data of Zhan et al. [39] for a net cage in current.

Sn	u_∞ [m/s]			
	0.25	0.5	0.75	1.0
0.128	−19.54	−14.68	−4.24	−0.94
0.215	−16.10	−21.14	−23.50	−20.58
0.223	16.86	−0.42	−1.54	−4.06

The considered experiments do not include measurements of the velocity reduction in and behind the cage. A typical velocity distribution is shown in Fig. 14 for $Sn = 0.128$ and $u_\infty = 0.5$ m/s. A gradual deceleration of the flow through the net cage is observed, whereas parts of the flow are accelerated along the sides of the cylindrical structure which leads to larger velocities than the inflow velocity outside the wake of the net cage.

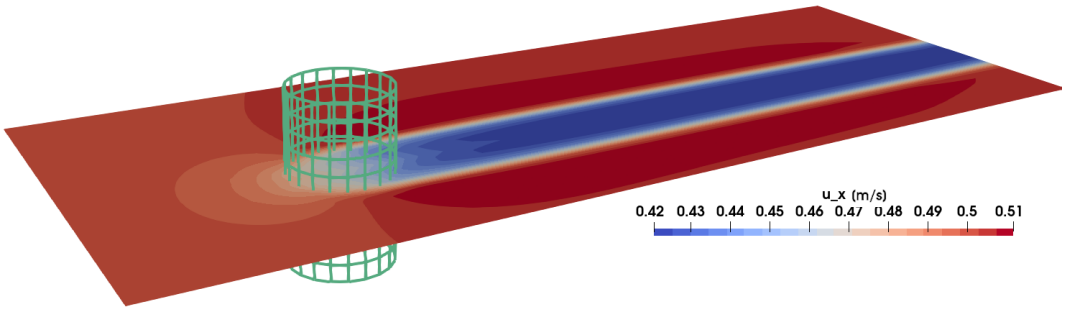

Figure 14: Numerical result for the x-velocity profile in the middle slice for the fixed net cage with $Sn = 0.128$ in steady current flow of $u_\infty = 0.5$ m/s.

6.4 Drag forces on a fixed net panel in regular waves

Lader et al. [24] presented an experimental study on the interaction of regular waves and net panels of different geometries. This allows testing of the proposed model in a space- and time-varying velocity field including a free surface. As pointed out by Kristiansen and Faltinsen [20], the screen force model is also applicable to wave cases because the KC number is large, i.e. quasi-steady flow conditions.

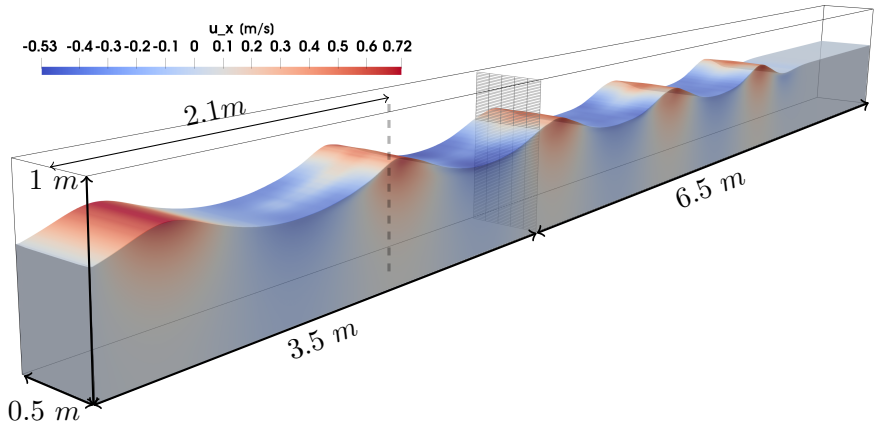

Figure 15: Computational domain for the simulation of a fixed net panel in regular waves. Colours show velocities in x-direction.

Table 10: Wave input parameters for the simulation of fixed net panels in waves (taken from [24]).

Wave case	1	2	3	4	5
Wave frequency f $[Hz]$	1.42	1.42	1.42	1.25	1.0
Wave height H $[m]$	0.045	0.064	0.084	0.104	0.167

The numerical wave tank is defined as shown in Fig. 15. It has a length of 10 m, a height of 1.0 m and a width of 0.5 m. The water depth is set to 0.62 m. The tank is shortened in comparison to the experimental wave flume to save computational time. A two wavelength long numerical beach is placed at the end of the tank to absorb the wave energy. A wave relaxation zone of one wavelength is defined at the inlet to generate waves. The numerical wave tank was thoroughly described in [8] and successfully validated for regular [18], irregular [2] and breaking waves [1]. In the experiments, five different regular waves of different length, height and steepness are generated using a vertical piston wavemaker. Fifth-order Stokes wave theory is used to model these waves because the wavemaker signal is not available and the Ursell numbers are small. The input wave frequencies and heights are given in Tab. 10. The investigated net panels have the same width and height as the tank and solidities of $0.095, 0.22$ and 0.288. They are referred as net case 1-3 in the following. The panel is placed 3.5 m in the tank. The time series for the drag forces and the wave elevation 1.4 m in front of the net are recorded for further analyses. A section of the series is compared to the measured time series in the Figs. 16 - 20.

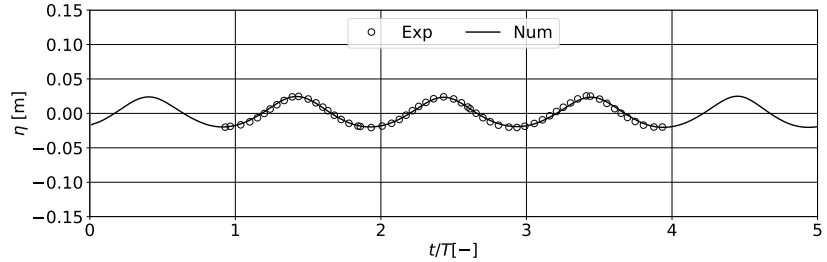

(a) Surface elevation at the wave gage.

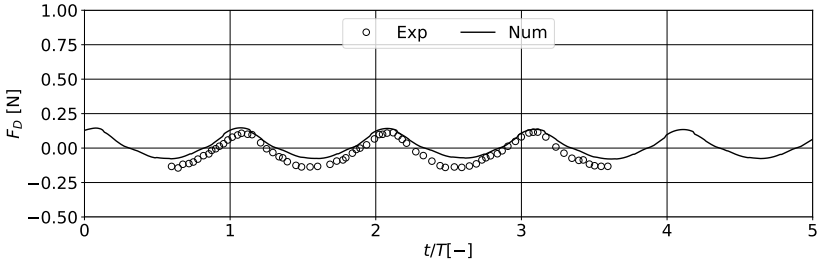

(b) Drag force for net case 1.

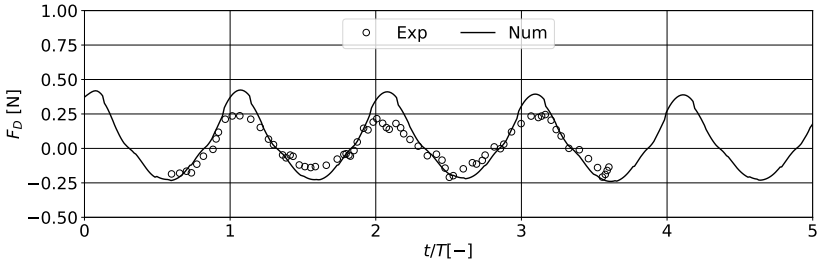

(c) Drag force for net case 2.

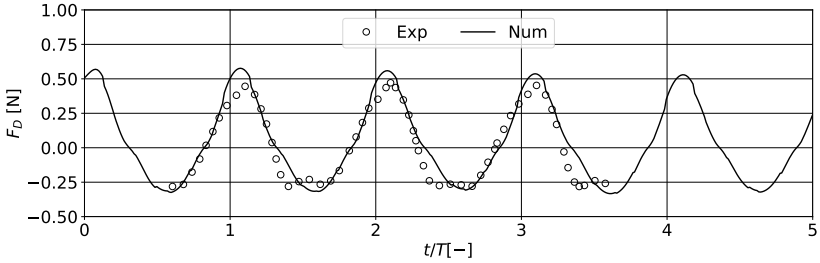

(d) Drag force for net case 3.

Figure 16: Numerical and experimental time series of surface elevation η and drag forces for wave case 1 with $f = 1.42\ Hz$ and $H = 0.045$ m.

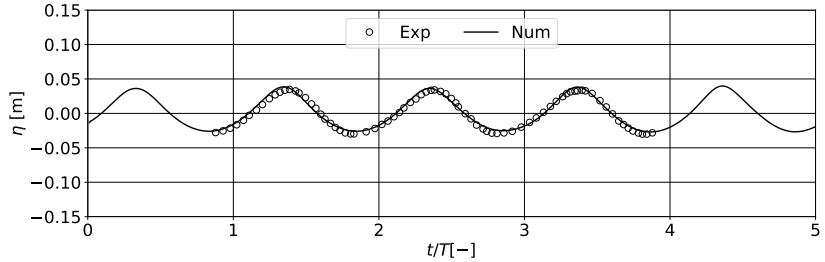

(a) Surface elevation at the wave gage.

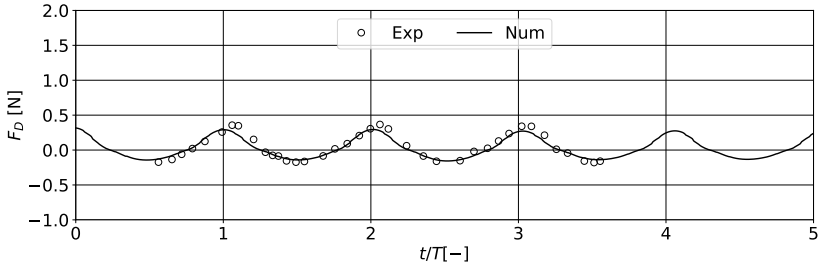

(b) Drag force for net case 1.

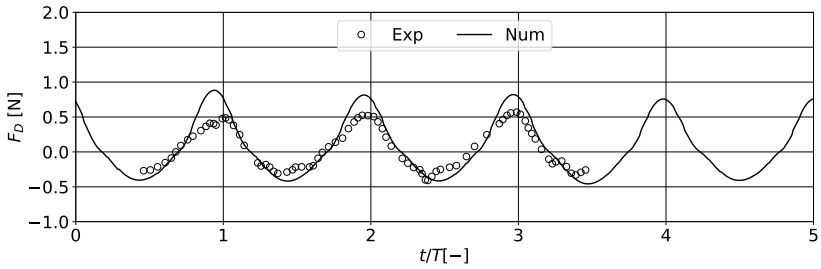

(c) Drag force for net case 2.

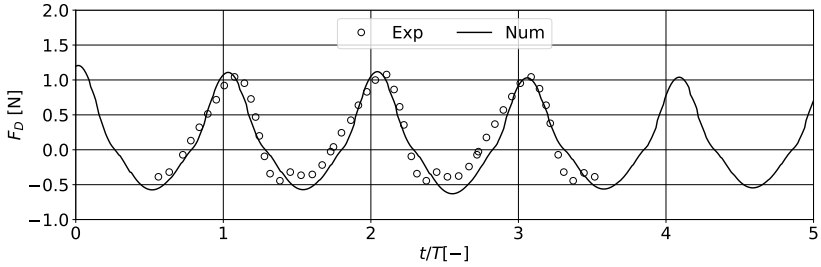

(d) Drag force for net case 3.

Figure 17: Numerical and experimental time series of surface elevation η and drag forces for wave case 2 with $f = 1.42\ Hz$ and $H = 0.064$ m.

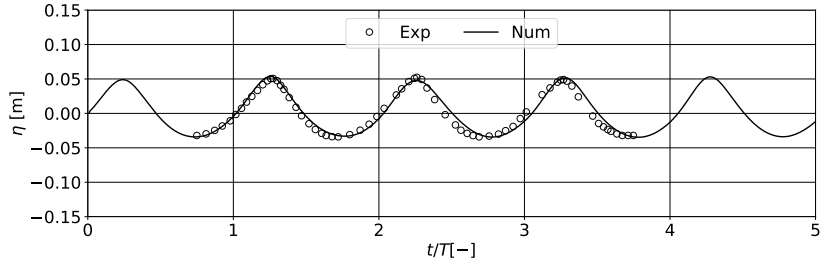

(a) Surface elevation at the wave gage.

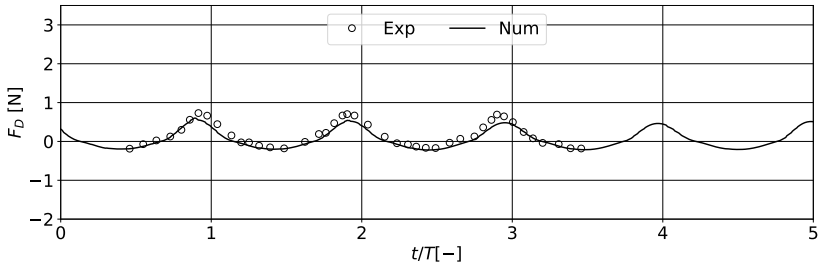

(b) Drag force for net case 1.

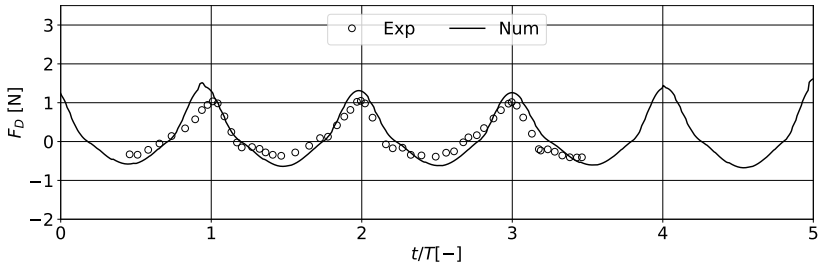

(c) Drag force for net case 2.

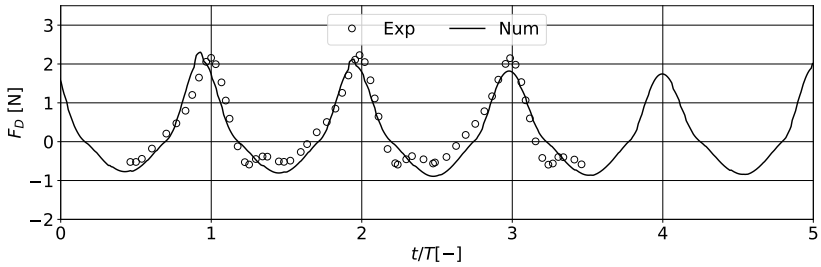

(d) Drag force for net case 3.

Figure 18: Numerical and experimental time series of surface elevation η and drag forces for wave case 3 with $f = 1.42\ Hz$ and $H = 0.084$ m.

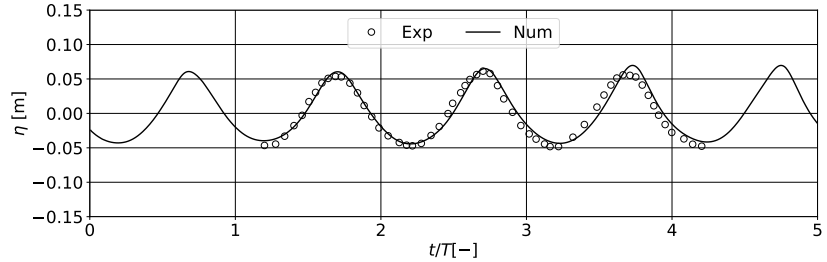

(a) Surface elevation at the wave gage.

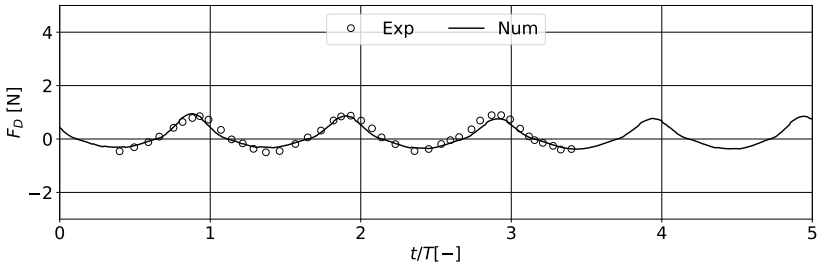

(b) Drag force for net case 1.

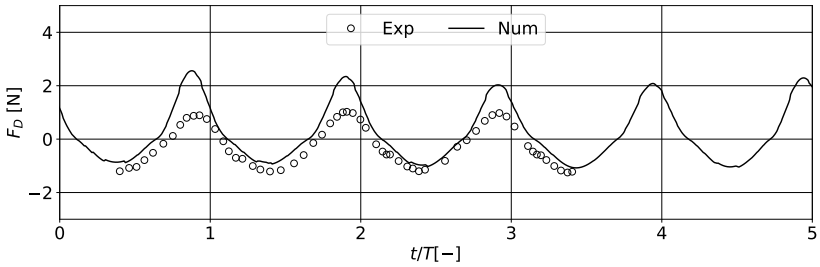

(c) Drag force for net case 2.

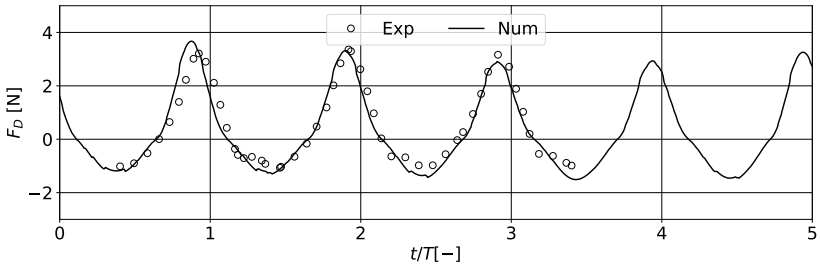

(d) Drag force for net case 3.

Figure 19: Numerical and experimental time series of surface elevation η and drag forces for wave case 4 with $f = 1.25\ Hz$ and $H = 0.104$ m.

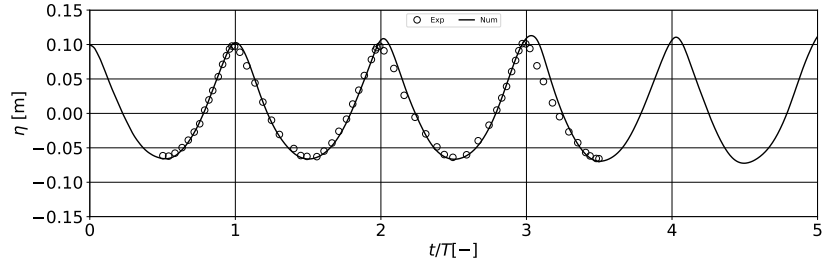

(a) Surface elevation at the wave gage.

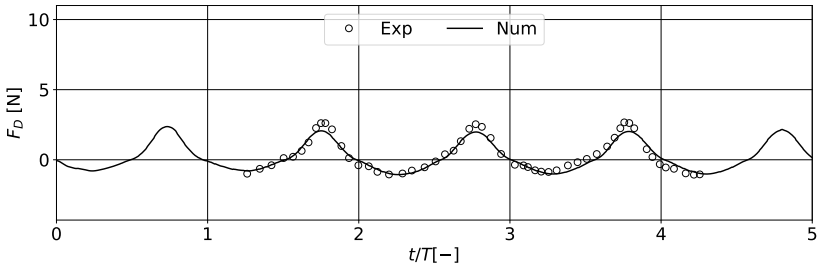

(b) Drag force for net case 1.

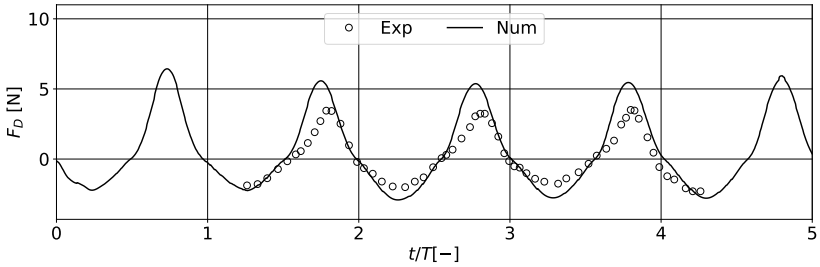

(c) Drag force for net case 2.

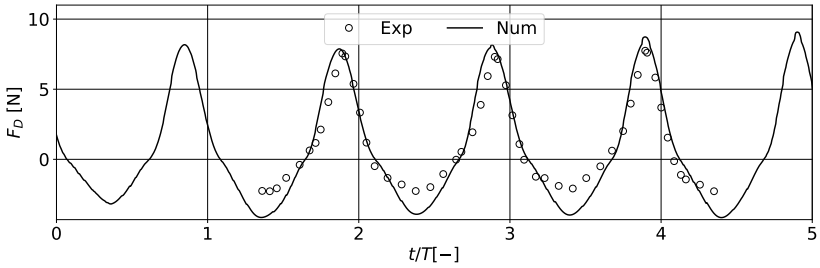

(d) Drag force for net case 3.

Figure 20: Numerical and experimental time series of surface elevation η and drag forces for wave case 5 with $f = 1.0\ Hz$ and $H = 0.167$ m.

In general, the numerically predicted wave propagation matches well with the experiments (Figs. 16a - 20a). Lader et al. [24] suggest evaluating the wave energy by calculating the zeroth-order moment of the power spectrum due to the non-linearity of the wave. Fig. 21 shows the amplitude spectra of the five simulated wave signals into their frequency components. They indicate the adequate representation of the low-order component (Stokes drift) and several

high-order components with multiple times the leading wave frequency. However, all these amplitude components are at most 1/5 of the leading wave frequency component. Thus, their contribution to the total wave energy is of minor interest, and it is justified to simplify the analysis to a comparison of the wave amplitudes. Following Lader et al. [24], a distinction between positive and negative amplitudes is made because of the asymmetry of the waves with higher crests and shallower troughs. As illustrated in Fig. 22b, the higher wave crests result in higher particle velocities and larger submerged net area. This corresponds to larger drag forces on the net in the wave propagation direction. In contrast, the load changes sign in a wave trough situation (Fig. 22a), and a smaller net area is wetted.

The most important components of the total wave forces act on the net with the regular wave frequency as shown in the Figs. 23a - 23e. Therefore, it is sufficient to compare the drag force amplitudes when the total wave forces are of interest. It is also noticed from these figures that the magnitude of the forces increases with the net solidity and wave amplitude. Both phenomena are expected from the validation cases.

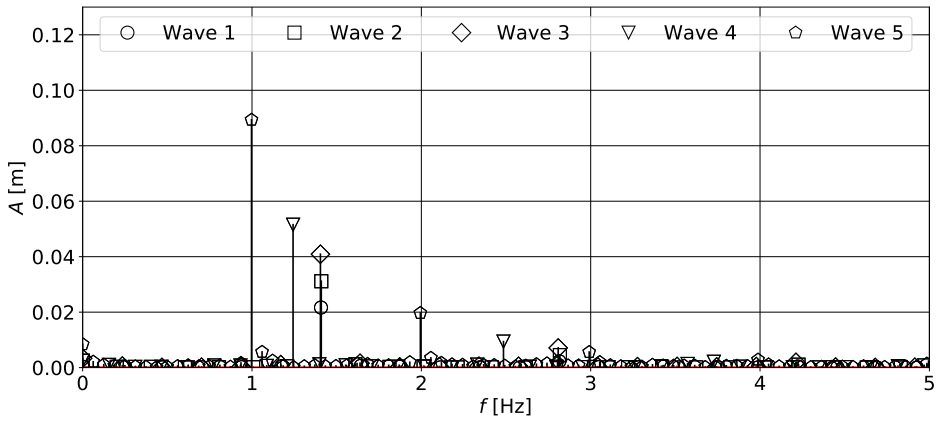

Figure 21: Amplitude spectra of the numerical wave elevation time series for the five different wave cases.

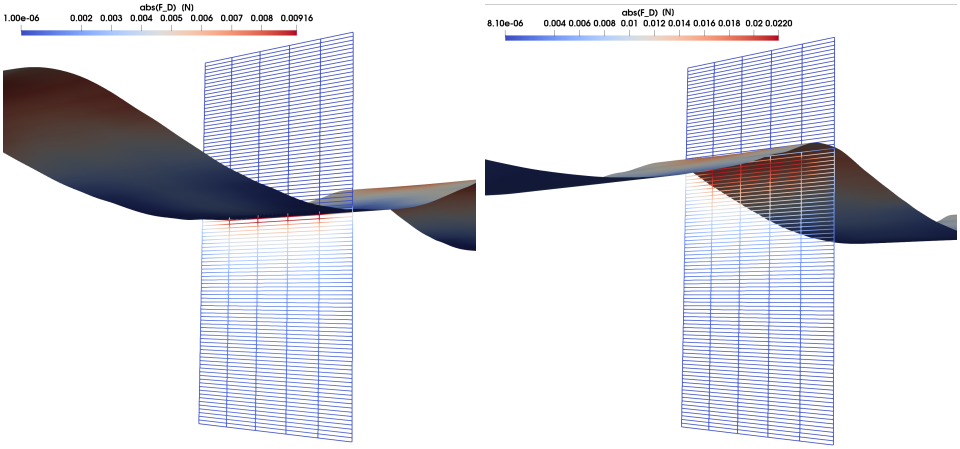

(a) Wave trough situation. (b) Wave crest situation.

Figure 22: Distribution of the drag force magnitudes on net panel with $Sn = 0.288$ in wave 5.

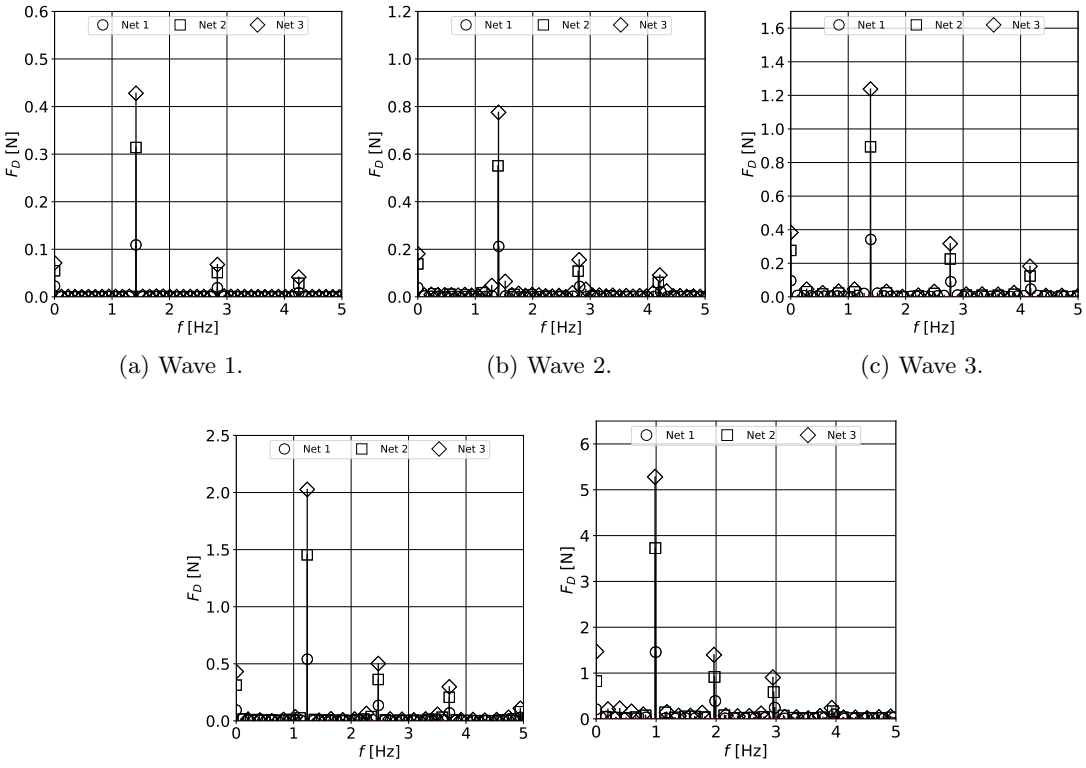

(a) Wave 1. (b) Wave 2. (c) Wave 3.

(d) Wave 4. (e) Wave 5.

Figure 23: Amplitude spectra of the numerical drag force time series for the five different wave cases.

The quantification of the predicted wave and force amplitudes is performed considering the

deviation for the positive and negative side separately. For the wave propagation, this corresponds to values of less than 13% for all wave crest amplitudes and less than 12% for all wave trough amplitudes. The deviations for the drag forces are presented in Tab. 11. The forces are mostly under-predicted by up to 25% for the first net with $Sn = 0.095$. In comparison, the model over-predicts the forces for the nets with higher solidities. The positive forces on the net with the highest solidity are generally predicted with high accuracy (12% and less) whereas the negative forces show larger discrepancies (up to 30%). The intermediate solidity is generally predicted the least accurate with most deviations between 20% and 40%. Chen and Christensen [12] noticed similar challenges with their porous medium model and pointed to uncertainties in the experimental data. In addition, it is noticeable that the second net geometry consists of the shortest twines. This confirms the observation in section 6.3 where the net cage in steady current with the shortest twines was most challenging for the model.

Table 11: Deviations [%] between numerical simulation and experimental data of Lader et al. [24] for the averaged positive (+) and negative (−) drag force amplitudes.

Sn	Wave case									
	1		2		3		4		5	
	+	-	+	-	+	-	+	-	+	-
0.095	11.4	19.1	25.1	−17.6	23.2	1.9	10.9	21.7	17.9	0.5
0.22	−80.5	−21.4	−31.2	−30.6	−29.2	−49.1	−59.8	−29.2	−41.1	−21.7
0.288	−12.4	−30.3	−3.2	−9.8	−3.2	−20.2	4.3	−30.4	−3.2	−55.8

6.5 Velocity reduction behind multiple net panels in steady current flows

A final validation case is the comparison to the experiments of Bi et al. [5]. They conducted PIV measurements of the fluid around a single and multiple fixed net panels in varying currents. They were carried out in a wave-current flume at the State Key Laboratory of Coastal and Offshore Engineering at the Dalian University of Technology, China. The flume has the dimensions 22 m × 0.45 m × 0.6 m and a water depth of 0.4 m. The net panel is $L = 0.3$ m long and wide. It is placed in the centre of the flume normal to the flow direction. A knotless net with square meshes and $Sn = 0.243$ is used. The inflow velocities u_∞ are 0.056 m/s, 0.113 m/s, 0.17 m/s and 0.226 m/s. In a first measurement series, up to three additional panels of the same size and geometry are placed in the wake of the first panel. The distance between each panel is one panel length. The velocity is measured one panel length behind the last panel for each configuration. In a second series, the wake velocities are measured at different locations between and behind up to $N = 4$ net panels for $u_\infty = 0.17$ m/s. An illustration of the computational domain is shown in Fig. 24. The length of the domain is 3.8 m which is long enough to avoid eventual reflections from the outlet. All probe points are taken from the experiment at which the origin is located in the middle of the first panel. The same argument as given in section 6.1 is used for the calculation of the wake velocity. Therefore, several probes with the same x location are computed, averaged and compared to the experiment. In contrast to the previous cases, $\kappa = 0.05$ is applied. Thus, the influence of the net is higher than in section 6.1 which is physically linked to a higher solidity. As the main results, Fig. 25 and the Tabs. 12 and 13 show the qualitative and quantitative comparisons for the velocity reduction factor U_r with the experiments. Further, the variation of the drag forces on the different net panels for different inflow velocities is provided in Fig. 26.

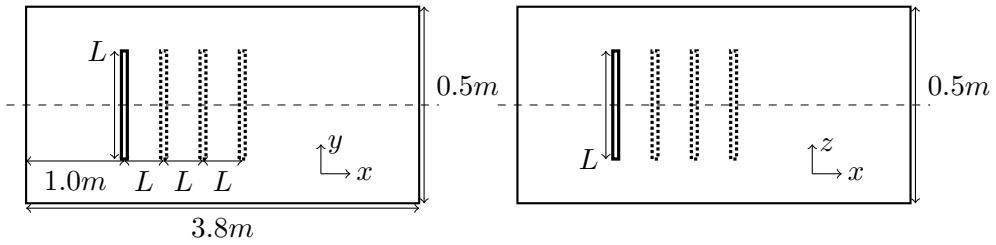

Figure 24: Computational domain for the simulation of multiple fixed net panels in steady current flow. Top view is shown on the left, side view is shown on the right. Origin of the coordinate system is on the intersection of the middle line and the first panel.

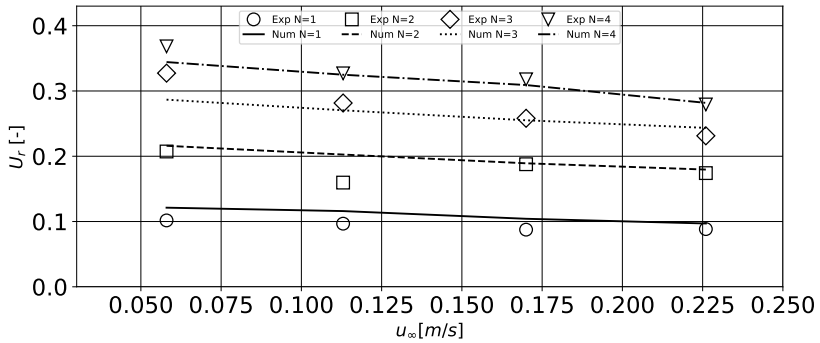

(a) Distribution of U_r over u_∞, measured 1.0 L behind the last panel.

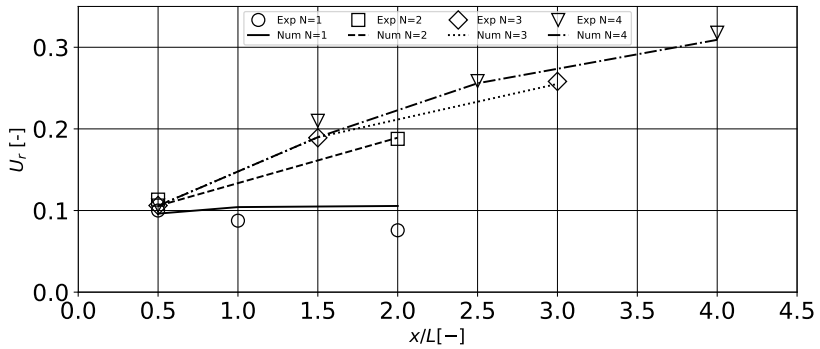

(b) Distribution of U_r over x/L for $u_\infty = 0.17$ m/s.

Figure 25: Comparison of the numerical and experimental velocity reduction factors for N fixed net panels in steady current flow.

As can be seen in Fig. 25a, the velocity reduction increases with the number of panels due to an increased resistance over the same distance. At the same time, U_r tends to decrease slightly if the inflow velocity is increased as can also be seen in the previous results (Fig. 10c). The quantitative analysis in Tab. 12 indicates a maximum deviation of 27%, but most deviations are well below 10%. Generally, the deviations are the largest for the single net case. However, $N = 1$ also results in the smallest reduction factors which correspond to the highest sensitivity to errors. If the L_2 norms of deviation, which are $0.033, 0.044, 0.044$ and 0.026 for

$N = 1 - 4$, are considered, it can be seen that the modelling deviation is similar for all cases. A further explanation can be obtained from Fig. 25b which presents the U_r distribution over $x/L = 0$ to $x/L = 4$ for $u_\infty = 0.17$ m/s and $N = 1 - 4$. In comparison to the velocity in the vicinity of the net, U_r slightly decreases over x. This effect implies an acceleration of the fluid which might be due to enhanced turbulence in the wake-field. In the numerical model, this would have to be incorporated by increasing the turbulence production through the net in the turbulence model. If multiple panels are arranged in such a way that the wake cannot evolve freely, as given in these computations, an increase of U_r can be observed (see also Fig. 27). As reported in [5], downstream panels slightly influence the flow through upstream panels which is also captured by the numerical model. This is confirmed by reporting the deviations in Tab. 13. All deviations are within a 10% deviation band for $N > 1$, and the L_2 norms of deviations are $0.034, 0.008, 0.003$ and 0.022 for $N = 1 - 4$.

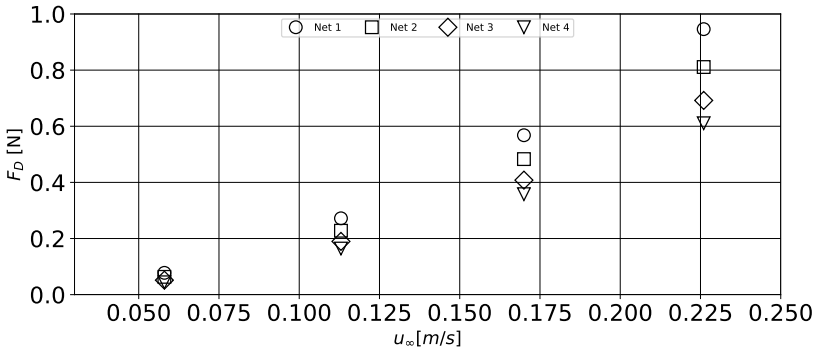

Figure 26: Numerical drag forces on four fixed net panels for varying steady inflow velocities.

The numerically predicted drag forces on the panels for different u_∞ and $N = 4$ are shown in Fig. 26. No measurements are available for comparison. The forces increase quadratically as a function of u_∞ for all nets as expected. Further, they decrease with the position of the corresponding net because of a decreased inflow velocity. It is also interesting to note that the difference in the calculated F_D between the first and the last net increases with u_∞. Thus, the importance of incorporating the velocity reduction behind a net increases with the inflow velocity.

Table 12: Deviations [%] for the velocity reduction factors measured 1.0 L behind the last net for different inflow velocities and varying number of panels N. The numerical results are compared to the experimental data of Bi et al. [5].

N	u_∞ [m/s]			
	0.058	0.113	0.17	0.226
1	−19.19	−19.94	−19.01	−9.71
2	−4.21	−26.90	−0.75	−3.10
3	12.41	3.97	1.18	−5.26
4	6.53	0.65	2.76	−0.88

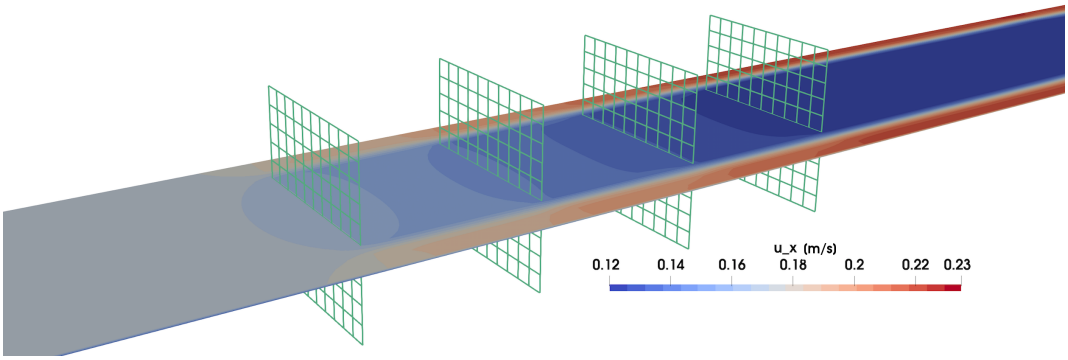

Figure 27: Numerical result for the x-velocity profile in the middle slice for 4 nets with $Sn = 0.243$ in steady current flow of $u_\infty = 0.17$ m/s.

Table 13: Deviations [%] for the velocity reduction factors at different x/L positions and varying number of panels N. The numerical results are compared to the experimental data of Bi et al. [5].

N	x/L [−]						
	0.5	1.0	1.5	2.0	2.5	3.0	4.0
1	3.80	−19.01	-	−39.47	-	-	-
2	6.75	-	-	−0.75	-	-	-
3	0.29	-	−0.29	-	-	1.18	-
4	0.29	-	9.60	-	1.04	-	2.76

7 Conclusions

The presented paper introduces a new method for modelling the flow through fish nets. The new approach is based on momentum disturbances incorporated into the Reynolds-averaged Navier-Stokes equations. The procedure is derived and discussed extensively. All necessary forces are calculated using the screen force model for plane net panels. This model has advantages over Morison type force models due to the incorporation of the angle between fluid and net into its formulation. The unknown force coefficients are determined from experimental data and a non-linear fitting algorithm. The new method represents the net as Lagrangian points in a Eulerian fluid domain. This simplifies the overall numerical procedure in comparison to porous medium models. Further, the disturbances are extrapolated on surrounding fluid cells but their origins are kept at the net itself. This is in contrast to a porous medium representation where the net is non-physically thickened. The transition from a surface force to a volume force leads to the introduction of a new parameter which has to be determined to account for the correct velocity reduction behind the net. The issue of transferring existing force models to coupled numerical simulations is discussed for the first time. The coupling process influences the flow velocity at the net which has to be corrected to match the undisturbed velocity used for computing force coefficients. An intrinsic formula is derived to couple these velocities using Froude's momentum theory. The numerical model is extensively validated against existing experiments for fixed net panels, multiple panels and cages with varying

geometries and solidities in current and regular waves. For all cases, both a qualitative and quantitative analysis is performed. Overall, the proposed model performs reasonably for all presented cases because deviation bands of less than 10% can be achieved regularly and physical explanations can be given elsewhere. This is true for both force coefficients and the velocity reductions in the wake.

The validation process indicates a possible limitation of the screen force model for nets with small twine lengths due to its assumptions. In particular, the applicability of the strip theory on each twine and the derived formula for the characteristic cross-flow velocity at the twines (see [14]) might have a constraint which is not discussed so far. Further, the presented computations indicate a dependency of κ on the net solidity but a low influence from varying inflow velocities or angles of attack. This simplifies the future work of finding a generally applicable formula for this parameter. The neglect of turbulence throughout the validation process indicates that this effect is not important for the correct modelling of loads. However, it plays a crucial role for investigations of the flow within net cages including fish and, therefore, turbulence modelling should be considered in the future. Besides, more validation for complex wave and current-wave conditions and the inclusion of net deformation will be considered.

Acknowledgements

The authors are grateful for the grants provided by the Research Council of Norway under the HAVBRUK2 project (no. 267981). This research was supported in part with computational resources at NTNU provided by NOTUR (Norwegian Metacenter for Computational Sciences, http://www.notur.no) under project no. NN2620K.

References

[1] A. Aggarwal et al. “Estimation of breaking wave properties and their interaction with a jacket structure”. In: *Journal of Fluids and Structures* 91 (2019). DOI: 102722.

[2] A. Aggarwal et al. “Free Surface Reconstruction for Phase Accurate Irregular Wave Generation”. In: *Journal of Marine Science and Engineering* 6 (3), 105 (2018). DOI: 10.3390/jmse6030105.

[3] N. Aquelet and J. Wang. “Porous parachute modelling with an Euler-Lagrange coupling”. In: *European Journal of Computational Mechanics* 16.3-4 (2007), pp. 385–399.

[4] C.-W. Bi et al. “Drag on and flow through the hydroid-fouled nets in currents”. In: *Ocean Engineering* 161 (2018), pp. 195–204.

[5] C.-W. Bi et al. “Experimental investigation of the reduction in flow velocity downstream from a fishing net”. In: *Aquaculture Engineering* 57 (2013), pp. 71–81.

[6] C.-W. Bi et al. “Numerical simulation of the interaction between flow and flexible nets”. In: *J. Fluids Struct.* 45 (2014), 180–201.

[7] H. Bihs and A. Kamath. “A combined level set/ghost cell immersed boundary representation for floating body simulations”. In: *Int. J. Numer. Meth. Fluids* Volume 83 (2017), 905–916.

[8] H. Bihs et al. "A new level set numerical wave tank with improved density interpolation for complex wave hydrodynamics". In: *Computers & Fluids* Volume 140 (2016), 191–208.

[9] J.U. Brackbill, D.B. Kothe, and C. Zemach. "A Continuum Method for Modeling Surface Tension". In: *Journal of Computational Physics* Volume 100(2) (1992), 335–354.

[10] J.S. Carlton. *Marine Propellers and Propulsion*. Fourth. Butterworth-Heinemann, Oxford, UK, 2019.

[11] H. Chen and E.D. Christensen. "Development of a numerical model for fluid-structure interaction analysis of flow through and around an aquaculture net cage". In: *Ocean Engineering* 142 (2017), 597–615.

[12] H. Chen and E.D. Christensen. "Investigations on the porous resistance coefficients for fishing net structures". In: *J. Fluids Struct.* 65 (2016), 76–107.

[13] A. Chorin. "Numerical solution of the Navier-Stokes equations". In: *Mathematics of Computation* Volume 22 (1968), 745–762.

[14] O.M. Faltinsen and A.N. Timokha. *Sloshing*. Cambridge University Press, 2009.

[15] A. Fredheim. *Current Forces on Net Structures*. Ph.D. thesis, NTNU Trondheim, Norway. 2005.

[16] G.S. Jiang and D. Peng. "Weighted ENO schemes for Hamilton Jacobi equations". In: *SIAM Journal of Scientific Computing* Volume 21 (2000), 2126–2143.

[17] G.S. Jiang and C.W. Shu. "Efficient implementation of weighted ENO schemes". In: *Journal of Computational Physics* Volume 126(1) (1996), 202–228.

[18] A. Kamath et al. "CFD Simulations of Wave Propagation and Shoaling over a Submerged Bar". In: *Aquatic Procedia* 4 (2015), pp. 308–316.

[19] T. Kristiansen and O. M. Faltinsen. "Experimental and numerical study of an aquaculture net cage with floater in waves and current". In: *Journal of Fluids and Structures* 54 (2015), pp. 1–26.

[20] T. Kristiansen and O. M. Faltinsen. "Modelling of current loads on aquaculture net cages". In: *Journal of Fluids and Structures* 34 (2012), pp. 218–235.

[21] P.F. Lader and B. Enerhaug. "Experimental Investigation of Forces and Geometry of a Net Cage in Uniform Flow". In: *IEEE Journal of Oceanic Engineering* 30.1 (2005), pp. 79–84.

[22] P.F. Lader and A. Fredheim. "Dynamic properties of a flexible net sheet in waves and current—A numerical approach". In: *Aquacultural Engineering* 35 (3) (2006), pp. 228–238.

[23] P.F. Lader et al. "Experimental Investigation of the Interaction between Waves and Net Structures—Damping Mechanism". In: *Aquacultural Engineering* 37.2 (2007), pp. 100–114.

[24] P.F. Lader et al. "Experimental Investigation of Wave Forces on Net Structures". In: *Applied Ocean Research* 29.3 (2007), pp. 112–127.

[25] G. Løland. *Current forces on and flow through fish farms*. Ph.D. thesis, NTH Trondheim, Norway. 1991.

[26] T. Martin et al. "Efficient implementation of a numerical model for flexible net structures". In: *Ocean Engineering* Volume 150 (2018), 272–279.

[27] J.A. Nelder and R. Mead. "A Simplex Method for Function Minimization". In: *The Computer Journal* 7 (4) (1965), pp. 308–313.

[28] S. Osher and J.A. Sethian. "Fronts propagating with curvature-dependent speed: Algorithms based on Hamilton-Jacobi formulations". In: *Journal of Computational Physics* Volume 79 (1988), 12–49.

[29] Ø. Patursson et al. "Development of a porous media model with application to flow through and around a net panel". In: *Ocean Engineering* 37 (2010), 314–324.

[30] C. S. Peskin. "Numerical analysis of blood flow in the heart". In: *Journal of Computational Physics* 25 (3) (1977), pp. 220–252.

[31] P.J. Roache. "Quantification of Uncertainty in Computational Fluid Dynamics". In: *Annu.Rev. Fluid Mech.* No. 29 (1997), pp. 123–160.

[32] H. Rudi, G. Løland, and I. Furunes. *Experiments With Nets; Forces on and Flow Through Net Panels and Cage Systems*. Technical Report MT51 F88-0215, MARINTEK, Trondheim, Norway. 1988.

[33] H. Schlichting and K. Gersten. *Boundary-Layer Theory*. Ninth. Springer-Verlag Berlin Heidelberg, Germany, 2017.

[34] C.W. Shu and S. Osher. "Efficient implementation of essentially non-oscillatory shock-capturing schemes". In: *Journal of Computational Physics* Volume 77(2) (1988), 439–471.

[35] M. Sussman, P. Smereka, and S. Osher. "A level set approach for computing solutions to incompressible two-phase flow". In: *Journal of Computational Physics* Volume 114 (1994), 146–159.

[36] I. Tsukrov et al. "Finite element modeling of net panels using a consistent net element". In: *Ocean Engineering* 30 (2003), pp. 251–270.

[37] H. van der Vorst. "BiCGStab: A fast and smoothly converging variant of Bi-CG for the solution of nonsymmetric linear systems". In: *SIAM Journal of Scientific Computing* Volume 13 (1992), 631–644.

[38] Y. Yao et al. "Numerical modeling of current loads on a net cage considering fluid–structure interaction". In: *Journal of Fluids and Structures* 62 (2016), pp. 350–366.

[39] J.M. Zhan et al. "Analytical and experimental investigation of drag on nets of fish cages". In: *Aquacultural Engineering* 35 (1) (2006), pp. 91–101.

[40] Y.-P. Zhao et al. "Numerical Simulation of Interaction Between Waves and Net Panel Using Porous Media Model". In: *Engineering Applications of Computational Fluid Mechanics* 8.1 (2014), pp. 116–126.